

UNCLASSIFIED



**Australian Government**  
**Department of Defence**  
Defence Science and  
Technology Organisation

## Bi-axial Vibration Energy Harvesting

*Scott Moss, Joshua McLeod, Ian Powlesland and Steve Galea*

**Air Vehicles Division**  
Defence Science and Technology Organisation

DSTO-TR-2649

### ABSTRACT

This report describes a vibration energy harvesting approach that uses a magnetoelectric (ME) transducer to harvest energy from bi-axial vibrations. The approach is being explored as a potential means of powering in situ structural health monitoring systems embedded within aircraft and other high value engineering assets that experience mechanical vibration. A bi-axial oscillator is created using a permanent-magnet/ball-bearing arrangement, which has the added benefit of permitting a relatively compact design. The magnet produces a bi-axial restoring force on the bearing, and as the bearing oscillates it steers a magnetic field through a magnetostrictive/piezoelectric laminate transducer thereby producing an oscillating charge that can be harvested. A simple laboratory demonstrator of a bi-axial ME harvester was created using a Terfenol-D/lead zirconate titanate/Terfenol-D transducer, and was shown to produce a peak rms power of 121  $\mu$ W from an rms acceleration of 61 mG at 9.8 Hz.

### RELEASE LIMITATION

*Approved for public release*

UNCLASSIFIED

UNCLASSIFIED

*Published by*

*Air Vehicles Division  
DSTO Defence Science and Technology Organisation  
506 Lorimer St  
Fishermans Bend, Victoria 3207 Australia*

*Telephone: (03) 9626 7000*

*Fax: (03) 9626 7999*

*© Commonwealth of Australia 2012*

*AR-015-202*

*July 2012*

**APPROVED FOR PUBLIC RELEASE**

UNCLASSIFIED

UNCLASSIFIED

# Bi-axial Vibration Energy Harvesting

## Executive Summary

In-situ Structural Health Monitoring (SHM) devices allow the Australian Defence Force to move from expensive time-based maintenance approaches for ageing platforms to cost-effective condition-based approaches. For air platforms the installation of these systems is complicated by the fact that the majority of SHM devices need to be fitted on internal aircraft structure, underneath the aircraft's skin. If the SHM device is in a location that is difficult to access, then powering the device may be problematic because traditional powering methods are in general not feasible. For example, replacing batteries on many SHM devices deployed across a fleet would be impractical, and accessing an on-board power system to supply SHM devices may lead to flight worthiness and certification issues. To address this powering issue the Australian Defence Science and Technology Organisation (DSTO) is investigating the possible use of vibration energy harvesting (VEH). Two unresolved scientific issues that inhibit the use of VEH on aircraft are: (i) the need for a wide operational frequency bandwidth to permit harvesting from the frequency-rich vibration that can be present on airframes, and (ii) the need for a multi-axial harvesting approach, since aircraft vibrations are typically not uni-axial. Previous collaborative work between the DSTO and the Active Materials Laboratory at UCLA addressed the first issue by developing the vibro-impacting energy harvesting approach which produced VEH over a broader operational bandwidth compared with many other harvester approaches, including harvesters that are currently commercially available. The second fundamental issue with most VEH approaches (again including all known commercial vibration energy harvesters) is that they are uni-directional, and hence can only harvest vibrational energy from host accelerations along a single axis. Therefore, while a considerable amount of scientific literature exists on the topic of VEH, none to date reports on a technique to effectively harvest from bi-axial host accelerations. This report describes a bi-axial approach that represents a significant advancement in VEH, specifically the approach increases the operational directionality from single-axis to 360 degrees in a plane. Furthermore, to the author's knowledge this is the first harvester design that uses a magnet/bearing cantilever analogue (replacing the cantilever design used by many harvesters described in the literature) potentially allowing a significant reduction in harvester volume. Finally, to the authors' knowledge the harvester described in this report is the first that uses an oscillating ball-bearing to create magnetic flux steering through a magnetoelectric laminate transducer to generate harvestable electrical power. This report will describe modelling of the bi-axial harvester, and will also report on a simple laboratory demonstrator that was developed as a proof of concept.

UNCLASSIFIED

UNCLASSIFIED

*This page intentionally blank*

UNCLASSIFIED

## Authors

### **Scott Moss**

Air Vehicles Division

*Scott Moss received a B.App.Sci. in Applied Physics in 1990 from the Royal Melbourne Institute of Technology, winning the Walter Boas Memorial Prize that year. He was a contract lecturer/tutor at RMIT during 1991-1992, studied towards a PhD at RMIT during 1993-1996 investigating electrical contacts to high temperature superconductors, was a Research Associate at the University of Wollongong in 1997 investigating Uranium doping of Bismuth HTS tapes, and a Junior Lecturer at the University of Tasmania in 1998-1999 teaching physics and electronics. His PhD was conferred in 1999, the same year he joined DSTO Air Vehicles Division to mainly work on the development of the 'smart patch' composite repair for the RAAF F/A-18. In 2003 he was awarded a Defence Science Fellowship and spent a year at UCLA investigating energy harvesting from aircraft structures. This work continues as an exploration of techniques for powering, and communicating with, structural health monitoring devices.*

---

### **Joshua McLeod**

Air Vehicles Division

*Joshua McLeod is currently three years into completing the double degree of Bachelor of Engineering (Robotics and Mechatronics) and Bachelor of Science (Computer Science and Software Engineering). He is on a one-year contract with DSTO Smart Structures and Advanced Diagnostic Group as an Industrial Based Learning student, where he is researching various vibration energy harvesting techniques.*

---

**Ian Powlesland**  
Air Vehicles Division

*Ian Powlesland joined the then Aeronautical Research Laboratories in 1972, and retired from the DSTO in 2010 to take up the role of an Emeritus Technical Advisor within the Smart Structures and Advanced Diagnostics Group. During his career Ian predominantly worked with structural testing instrumentation which included early dedicated portable signal averaging equipment, Nomad, CT4 and F18 fatigue test control systems and some field trials. Currently he is working in the field of autonomous damage and loading sensors for managing an aging fleet.*

---

**Steve Galea**  
Air Vehicles Division

*Dr Galea graduated in 1980 with a Bachelor of Engineering (Mech.) from the University of Queensland with first class honours and in 1983 he received a Masters of Engineering Science. He commenced employment with the Aeronautical Research Laboratory in 1983. In 1985 he commenced studies at the Institute of Sound and Vibration Research, University of Southampton, UK and received his Doctor of Philosophy from the University of Southampton in 1989. Dr Galea is currently a Principal Research Scientist and Functional Head of the Smart Structures and Advanced Diagnostics Group. His current responsibilities involve the management of research and providing technical leadership on the development and application of smart materials and structures technologies to aircraft structures, including in-situ structural health monitoring and self-powering techniques. He has an extensive publication record of over 80 publications, which include three book chapters on smart structures and repairs to acoustically-fatigued structures.*

---

# Contents

<b>1. BACKGROUND.....</b>	<b>1</b>
<b>1.1 Magnetostriction, piezoelectricity, the magnetoelectric effect, and         magnetostrictive/piezoelectric lamina composites.....</b>	<b>2</b>
<b>1.2 Vibration energy harvesting.....</b>	<b>3</b>
<b>2. MODELLING.....</b>	<b>4</b>
<b>2.1 Two dimensional modelling.....</b>	<b>5</b>
<b>2.2 Three dimensional modelling.....</b>	<b>6</b>
<b>3. EXPERIMENTAL .....</b>	<b>7</b>
<b>4. RESULTS AND DISCUSSION .....</b>	<b>11</b>
<b>4.1 Mechanical and magnetostatic predictions.....</b>	<b>11</b>
4.1.1 Restoring force predictions .....	11
4.1.2 Magnetic field predictions.....	13
4.1.3 Qualitative stress modelling .....	17
4.1.4 Scaling laws for the bi-axial vibration energy harvester.....	19
<b>4.2 Electro-mechanical measurements .....</b>	<b>19</b>
4.2.1 Impedance as a function of frequency.....	19
4.2.2 Magnetoelectric voltage and bearing displacements as a function of frequency and drive angle .....	21
4.2.3 Magnetoelectric voltage as a function of host acceleration .....	23
4.2.4 Harvester output power as a function of load resistance .....	23
<b>4.3 Future work.....</b>	<b>24</b>
<b>5. CONCLUSION .....</b>	<b>25</b>
<b>6. REFERENCES .....</b>	<b>26</b>
<b>APPENDIX A: TWO-DIMENSIONAL MODELLING .....</b>	<b>30</b>
<b>APPENDIX B: THREE-DIMENSIONAL MODELLING .....</b>	<b>41</b>

UNCLASSIFIED

DSTO-TR-2649

*This page is intentionally blank*

UNCLASSIFIED



# 1. Background

The Australian Defence Science and Technology Organisation (DSTO) is developing a variety of in-situ structural health monitoring (SHM) approaches [1, 2, 3, 4, 5] for potential use in high value platforms across the Australian Defence Force. The SHM systems under development could be employed to: (i) continuously monitor airframe loads and accelerations during flight, (ii) detect damage and damage growth and other structural problems, and (iii) provide a basis for near-real-time damage assessment. This technology could also potentially permit a safe reduction in inspection and regular maintenance costs and therefore reduce aircraft through-life support costs.

DSTO is currently investigating the various components of the generic SHM concept depicted in Figure 1. The concept involves three main components, being: (i) a sensor mounted inside the aircraft at a difficult-to-access location, that is monitoring in-flight mechanical loads on an airframe [5], (ii) with the sensor utilising energy that is parasitically harvested from local airframe vibrations by an energy harvester [6, 7, 8, 9], and (iii) when the aircraft is on the ground a wireless link, the acoustic electric feedthrough, is used to download sensor data and to simultaneously provide additional energy to the sensor unit [10, 11, 12, 13, 14].

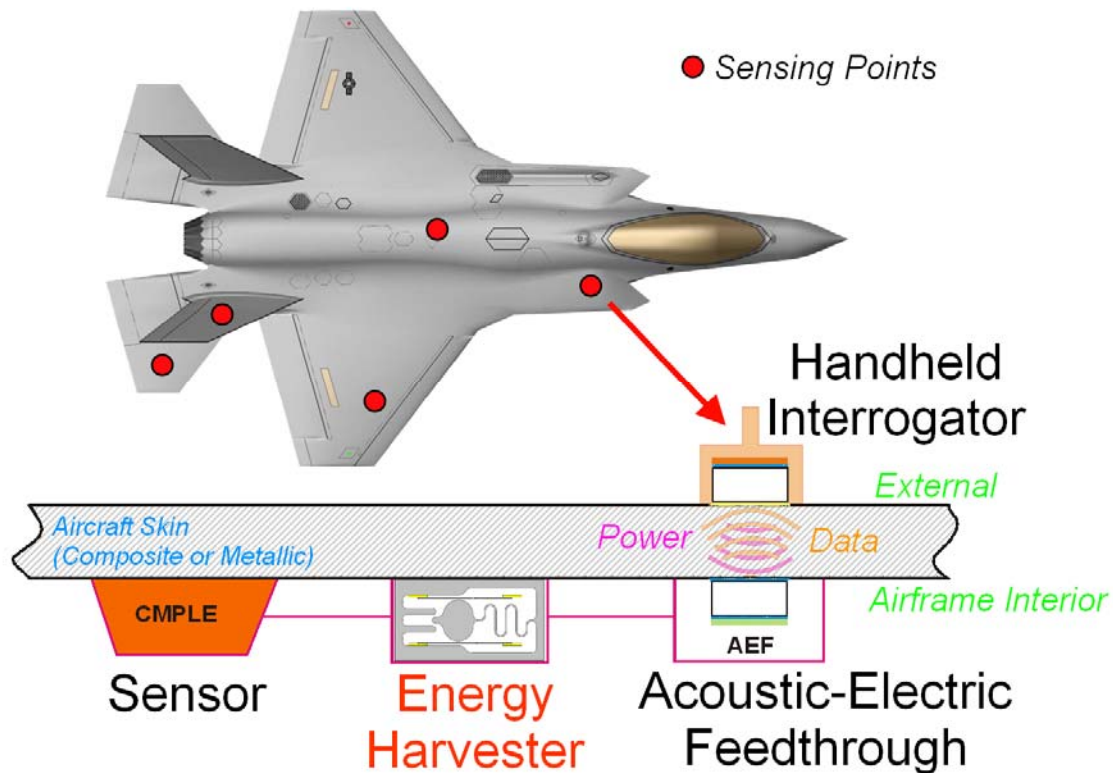


Figure 1. Schematic of a wireless Structural Health Monitoring system concept with sensing unit, energy harvester and wireless data and power transfer capability

## 1.1 Magnetostriction, piezoelectricity, the magnetoelectric effect, and magnetostrictive/piezoelectric lamina composites

In 1847 Joule observed that “the elongation is proportional, in a given [ferromagnetic] bar, to the square of the magnetic intensity” [15], the behaviour was termed the ‘Joule Effect’ and became known as magnetostriction. Somewhat later the reciprocal behaviour (or the inverse magnetostrictive effect) was discovered by Villari, who found that when a mechanical stress is applied to a ferromagnetic material that a change in magnetisation is produced [16]. In the 1970’s a magnetostrictive alloy with the formula  $Tb_xDy_{1-x}Fe_2$  ( $x \sim 0.3$ ) was discovered by researchers at the U.S. Naval Ordnance Laboratory. The alloy was named Terfenol-D after the laboratory (nol) and also its constitutive elements, terbium (ter), iron (fe) and dysprosium (D). The alloy exhibits what is known as the ‘giant magnetostrictive effect’, producing strains hundreds of times larger than those of classical magnetostrictive materials such as iron [17].

In 1880 the Curie brothers demonstrated the direct piezoelectric effect, finding that an applied mechanical stress could produce electrical charge in a solid [18]. The reciprocal behaviour (or the reverse piezoelectric effect) was mathematically deduced by Lippman’s discussion of fundamental thermodynamic conservation laws in reference [19]. Physicists at the Tokyo Institute of Technology investigated various piezoceramic materials [20], developing lead zirconate titanate (PZT) in around 1952. Reference [16] describes PZT as “the most common ferroelectric compound employed for smart material applications”, in part because of its high electromechanical coupling and extended operating temperature range.

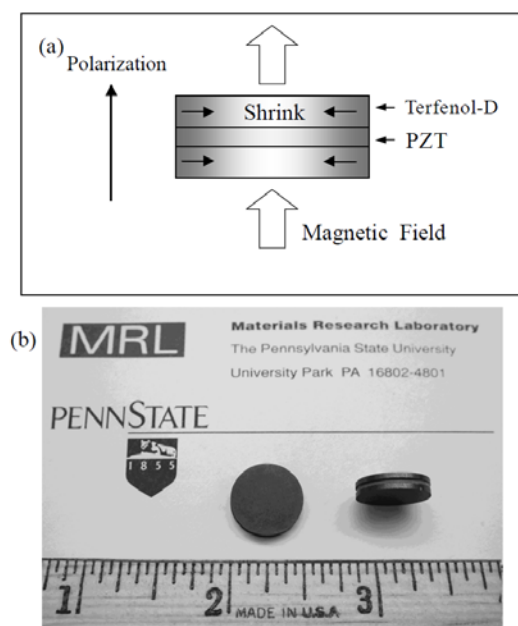


Figure 2. Magnetolectric lamina composites using Terfenol-D and PZT disks, as described by Ryu et al [25]. (Reproduced with permission, Japanese Society of Applied Physics).

The linear magnetoelectric (ME) effect describes the induction of magnetisation by an electric field, or the reverse effect of electric polarisation by a magnetic field. The history of discovery of the ME effect is well described in reference [21]. The effect was termed such by Debye in

1926 [22] after earlier work by Roentgen [23] and Curie [24]. In 2001 Ryu *et al* [25] developed a magnetostrictive/piezoelectric lamina composite with a ME voltage coefficient of  $4.68 \text{ V cm}^{-1} \text{ Oe}^{-1}$ ; the coefficient was 36 times greater than any previously reported ME particulate composite. Figure 2 is reproduced from Ryu's article, with Figure 2a depicting the behaviour of a Terfenol-D/PZT laminate under an applied magnetic field. Reference [25] develops an expression for the (open circuit) output voltage generated by an ME transducer subject to a stress in the direction orthogonal (i.e. the 1-direction, or  $y$ -axis) to the direction of polarisation (i.e. the '3-direction', or  $z$ -axis),

$$V_{OUT} = 2 \times g_{31} \times t_p \times \sigma_{31p}^E, \quad (1)$$

where  $g_{31}$  is the piezoelectric voltage constant ( $\text{Vm/N}$ ),  $t_p$  is the thickness of the PZT layer (m), and  $\sigma_{31p}^E$  is the mechanical stress in the PZT 1-direction (Pa).

## 1.2 Vibration energy harvesting

The use of parasitically harvested energy to power small sensor systems has become viable over the past decade due to the ever-decreasing power requirements of electronic devices [26]. This has resulted in considerable scientific interest in energy harvesting technologies [27, 28]. In particular, there has been significant interest in the area of vibration energy harvesting (VEH) [29], particularly for single-degree-of-freedom [30] (SDOF) piezoelectric [31] and magnetic [32] harvesters. Although there are a number of commercially available SDOF harvesters [27], there exist a number of continuing challenges that prevent widespread application of VEH such as limited operational frequency bandwidth [9] and low power density [33]. In many practical applications the direction of the incident vibration may vary, so another challenge is the uni-axial nature of many harvesters [34] particularly cantilever-based piezoelectric designs [35] and SDOF electromagnetic designs [36]. The magnetoelectric (ME) effect produced via magnetostrictive/piezoelectric laminates [37] has been used recently in a number of VEH studies [38]. In particular, a recent investigation [39] employed a cantilever arrangement with a tip-mass consisting of two pairs of rare-earth (NdFeB) magnets, that oscillates around a fixed Terfenol-D/PbTiO<sub>3</sub> laminate transducer. The uni-axial harvester examined in reference [39], with a single laminate transducer, produced  $\sim 100 \text{ } \mu\text{W}$  from a  $\sim 33 \text{ Hz}$ ,  $100 \text{ mG}$  excitation (assumed to be an rms acceleration).

This report describes an inherently compact bi-axial VEH approach that has been developed by DSTO [40]. The approach uses a permanent-magnet/ball-bearing combination, that operates in conjunction with a Terfenol-D/PZT laminate transducer (hereafter called the 'ME transducer'). On the 4th May 2011, the DSTO secured U.S. provisional patent protection on the bi-axial harvesting approach described in this report [41].

## 2. Modelling

This section examines the two and three-dimensional models developed to investigate the bi-axial harvester described in reference [41], which describes three nominal harvester types. This report will detail one of the harvester types, which has an ME transducer located between a ball-bearing (hereafter called the 'bearing') and a magnet. An artist's impression of what this type of harvester might look like in practice is shown in Figure 3.

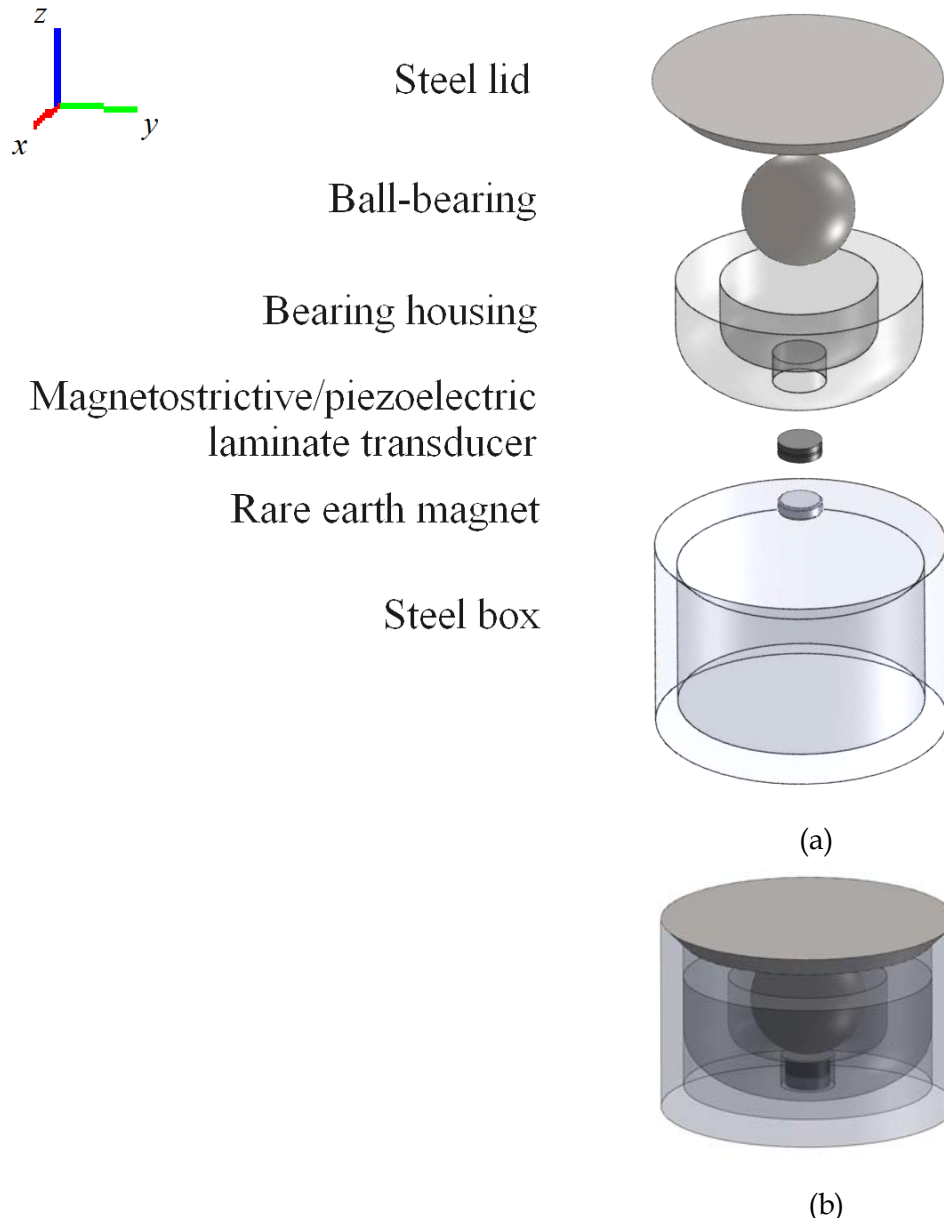


Figure 3. Artist's impression of the bi-axial vibration energy harvester examined in this report. Shown in (a) is an exploded view of the hypothetical harvester, and in (b) a view of the assembled harvester.

The bearing shown in Figure 3 is subject to a magnetic restoring force in the  $x$ - $y$  plane, however is otherwise free to move across the surface of the bearing housing in response to host structure oscillations. Comsol [42] multi-physics software was used to make predictions about the restoring force, and also about the magnetic field distribution as the bearing location changes.

## 2.1 Two dimensional modelling

A two-dimensional model was created based on the arrangement shown in Figure 4. This arrangement was chosen since it reflected the geometry of the device that was built to demonstrate the principle of the bi-axial ME harvester (the device will be described in detail in Section 3 of this report). Note that the central-line of the harvester is defined as the vertical line ( $z$ -direction) through the centre of the magnet (as shown in Figure 4). Rotational effects were ignored.

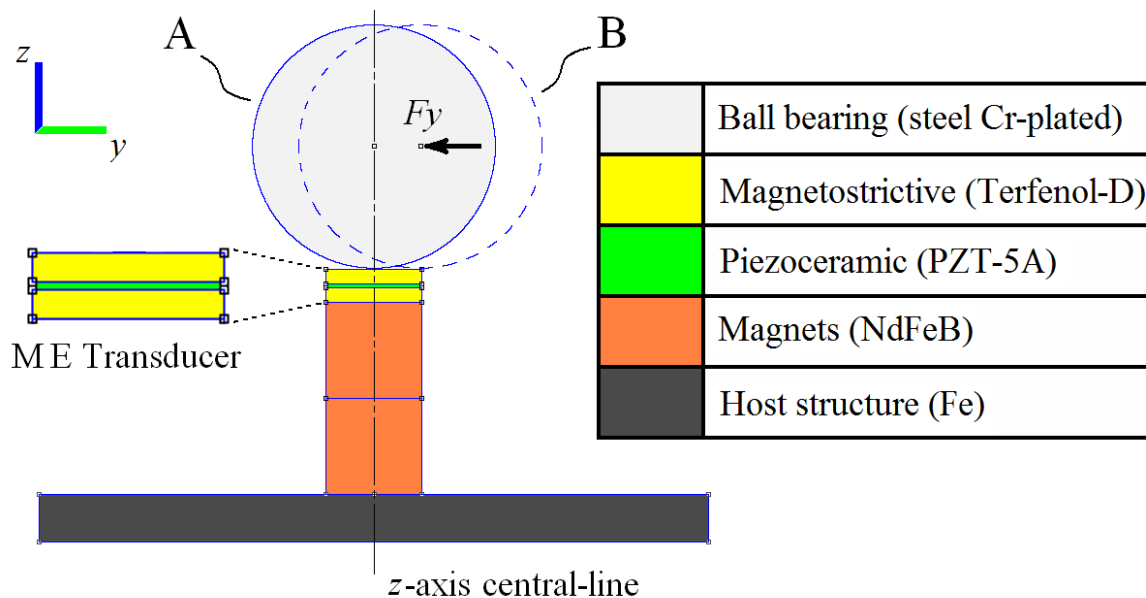


Figure 4. Two-dimensional schematic diagram of the bi-axial energy harvester, showing the magnetoelectric (ME) transducer located between the bearing and the magnet. Also shown is the bearing in its central rest position (A) and the magnetic restoring force  $F_y$ , acting on the displaced bearing (B). The bearing has a diameter of 25.4 mm. (Originally published in reference [40]).

The model was analysed using Comsol, allowing predictions of the static magnetic field distribution to be made (for various bearing positions). Of particular interest is the distribution of magnetic flux  $B$  in the ME transducer since this determines the stress distribution in the transducer, and hence the voltage generated. The Comsol application mode 'perpendicular induction currents, vector potential' was used to calculate the static magnetic field distribution for various bearing locations. In particular, the calculated magnetic fields were obtained from the static partial differential formulation of Ampere's law [43],

$$\nabla \times (\mu_0^{-1} \nabla \times A - M) - \sigma \nabla V = J^e, \quad (2)$$

where  $M$  is the in-plane ( $y$ - $z$ ) magnetisation vector,  $A$  is the magnetic vector potential,  $V$  is the electric potential,  $\sigma$  is the electric conductivity,  $\mu_0$  is the permeability of a vacuum, and  $J^e$  is the vector current density.

Two-dimensional modelling of the Terfenol-D nonlinear magnetostrictive response was carried out using an approach adapted from reference [44], which uses the phenomenological magnetostrictive equations [45, 46]. The deformation due to magnetostriction can be obtained using the following equation,

$$\frac{\delta l}{l} = \frac{3}{2} \lambda_s \left( \cos^2 \theta - \frac{1}{3} \right), \quad (3)$$

where  $l$  is the length of magnetostrictive material,  $\lambda_s$  is a constant representing the magnetostrictive deformation at saturation, and  $\theta$  is the angle between the directions of magnetisation and deformation. Lee, in reference [45], states that equation (3) “seems to hold fairly well for polycrystalline samples containing no preferred orientation of crystal axes”. Polycrystalline Terfenol-D satisfies this criterion since it is nominally isotropic. The directional term can be rewritten as the fraction of magnetisation with respect to saturation magnetisation thus,

$$\frac{\delta l}{l} = \frac{3}{2} \lambda_s \left( \left( \frac{I}{I_s} \right)^2 - \frac{1}{3} \right), \quad (4)$$

where  $I$  is the magnetisation and  $I_s$  is the magnetisation at saturation. The  $1/3$  term takes into account the magnetisation required to align the individual domains within the magnetostrictive material, and for this model it is ignored. This assumes that all domains are aligned, and furthermore are aligned perpendicular with the direction of magnetisation for maximum deformation.

The two-dimensional modelling undertaken in this report may be considered qualitative due to the (necessary) approximation that the ME transducer, and also the magnets, are uniformly 10 mm deep (instead of cylindrical). Furthermore, the two-dimensional model assumes that the piezoelectric response is isotropic, and mechanical only (i.e. no electromechanical effects, the piezoceramic is in a short-circuit condition). A detailed discussion of the two-dimensional modelling methodology can be found in Appendix A (Table A3 containing relevant material properties, using silver-epoxy properties given in [47]).

## 2.2 Three dimensional modelling

Due to the cylindrical geometry of the magnets a three-dimensional model was required to obtain reasonably accurate predictions of bearing restoring force (and also of strain in the piezoelectric layer of the ME transducer, which is to be reported in future work). Specifically,

the two-dimensional arrangement shown in Figure 4 was extended into three-dimensions, as shown in Figure 5. A three dimensional model was developed using the Comsol application mode '*magnetostatics, no currents*', the geometry of which is shown in Figure 5. The model was analysed using Comsol driven by a Matlab script [48]. To find the total magnetic force acting on the bearing, the Maxwell stress tensor [49] must be calculated. Comsol employs the following projection of the Maxwell stress tensor onto the outside surface of the bearing [43],

$$n_1 T_2 = -p n_1 - \left(\frac{1}{2} E \cdot D + \frac{1}{2} H \cdot B\right) n_1 + (n_1 \cdot E) D^T + (n_1 \cdot H) B^T \quad (5)$$

where  $n_1$  is the surface normal vector pointing out from the surface of the bearing,  $p$  is the air pressure,  $D = \epsilon E$  is the electric displacement,  $B = \mu H$  is the magnetic flux density,  $\mu$  and  $\epsilon$  are the permeability and permittivity respectively. Note that  $n_1$ ,  $E$  the electric field, and  $H$  the magnetic field intensity, are all 1-by-3 vectors. Comsol uses equation (5) directly in the boundary integral of the stress tensor to compute the total force on the bearing. Magnetic force predictions were made assuming that the ME transducer acted as a 3.5 mm air gap between the magnet and the bearing (i.e. the force predictions ignore the effect of the ME transducer). The assumption that the ME transducer acted as a gap between the magnet and the bearing was considered reasonable since it was found that including the ME transducer in the three-dimensional model did not significantly alter the predicted restoring force,  $F_y$ . Stable finite element solutions were obtained if the maximum element dimension chosen was 1.5 mm or less, and also if the meshing of the magnet and bearing was sufficiently refined. A detailed discussion of the three-dimensional modelling methodology can be found in Appendix B.

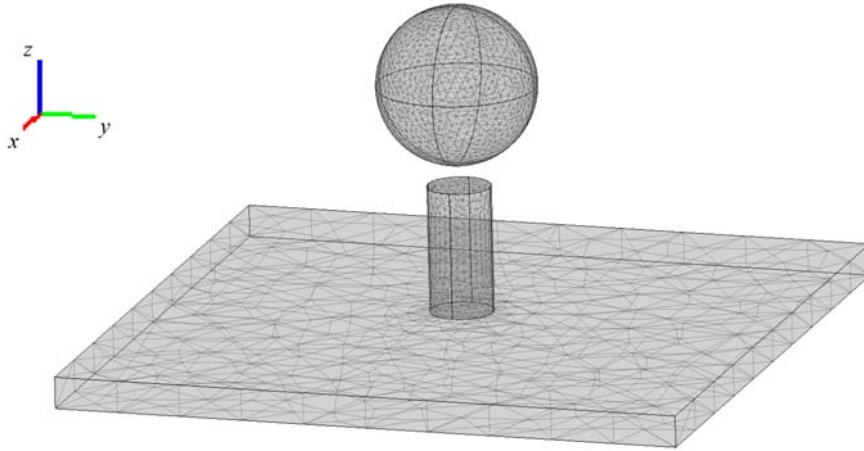


Figure 5. Three-dimensional model showing the bearing elevated 3.5 mm above the magnet surface

### 3. Experimental

A simple device was built to demonstrate the principle of bi-axial ME vibration energy harvesting. Figure 6a is a photograph of the permanent-magnet/bearing oscillator arrangement, and shows the ME transducer located between the bearing and the magnet. The steel bearing (grade AISI 52100) is spherical with a diameter of 25.4 mm; the rare-earth

magnets (NdFeB, grade N42) and the ME transducer are cylindrical, and have a diameter of 10 mm.

The ME transducer was formed by bonding the Terfenol-D (Etrema Products Inc.) and PZT elements (Pz27, Ferroperm Piezoceramics A/S), both 10 mm diameter, with silver loaded epoxy (CW2400, Circuitworks) that was cured for two hours at 55 °C under a compressive load of ~1 MPa. Reference [25] indicates that the output from an ME lamina composite transducer may be optimised by choosing magnetostrictive and piezoelectric layers with a thickness ratio of approximately three to one. Hence the Terfenol-D and PZT layers of the ME transducer were chosen to be 1.5 mm and 0.5 mm thick respectively. The host structure oscillates in the  $x$ - $y$  plane (Figure 5). The magnets and the piezoceramic are poled in the  $z$ -direction. The magnets are 10 mm thick, and for experimental convenience two magnets were stacked together (for a total magnet thickness of 20 mm), and attached to a 5 mm thick steel base using magnetic force. A thin layer of beeswax [50] was employed at the interface between the ME transducer and the upper magnet to minimise shear movement.

Measurements of the PZT element impedance were made before and after bonding into the lamina composite, using the approach described in reference [10]. The results of the impedance measurement are presented in Section 4, however it is noted that the measured capacitance of ME transducer (i.e. the bonded PZT element) was 1.86 nF at 10 Hz.

Figures 6a and 6b depict the experimental arrangement, showing the harvester attached to a 5 g steel host mass (hanging from two wire ligaments), connected to a 75 N vibration shaker (TIRA S 511 75 N). Host accelerations were measured using an accelerometer (PCB 333B40), and a laser displacement sensor was used to measure the bearing displacement ( $y$ -direction) during testing (ODS 115 Black-line). Care was required when aligning the laser; for reliable displacement measurements the laser had to be aimed at the centre of the bearing parallel with the direction of the host acceleration. A maximum rms host acceleration of 61 mG was chosen because, at resonance, larger host accelerations would drive the bearing off the edge of the ME transducer. It is worth noting, as indicated in Figure 3, that future work will use a cylindrical housing to constrain the bearing displacement and to also introduce a two-dimensional vibro-impact effect that may lead to increased operational frequency bandwidth [9].



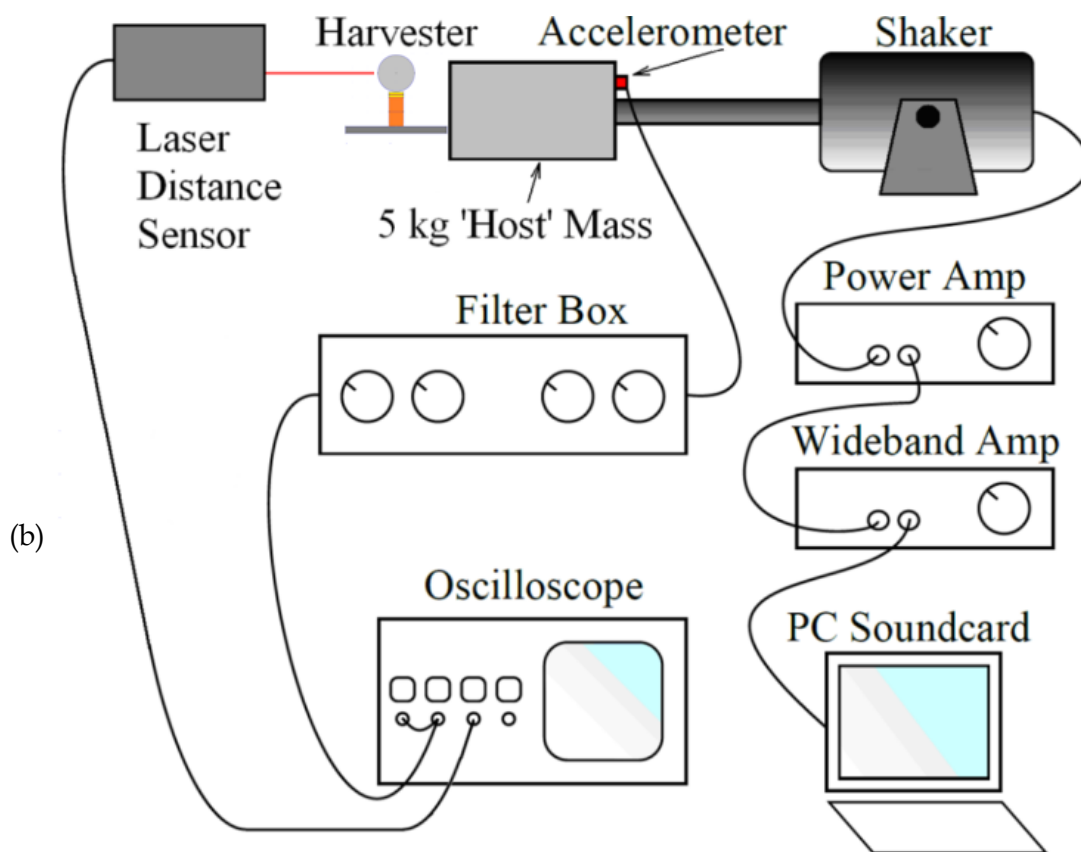
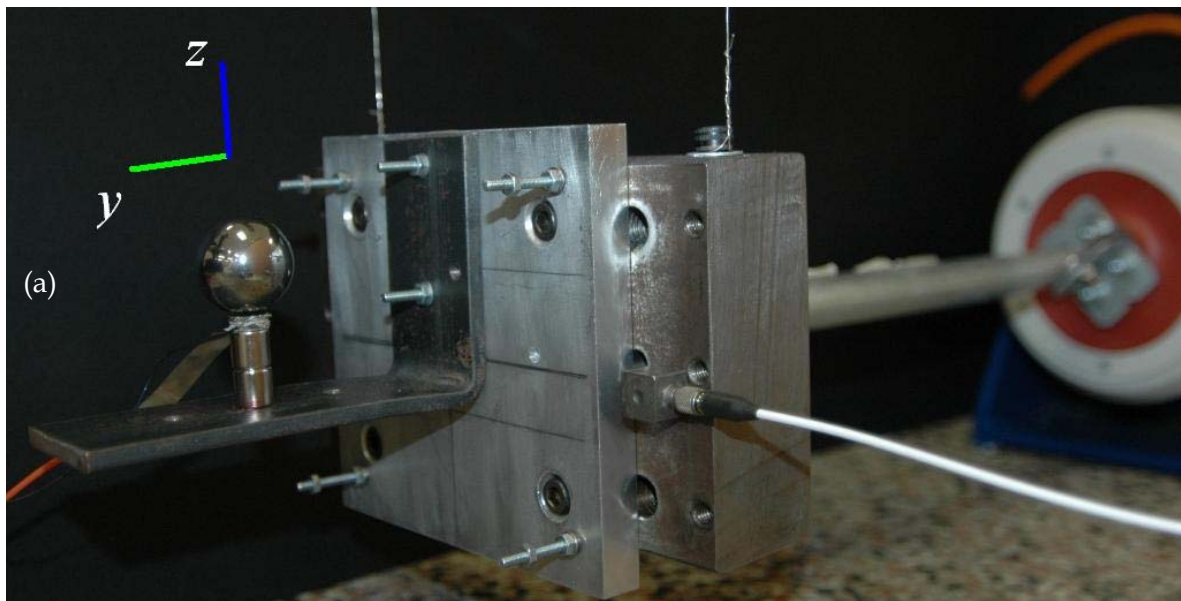


Figure 6. (a) Photo (originally published in reference [40]), and (b) schematic, of the experimental arrangement

Two electrical connections were made to the ME transducer, one at the top Terfenol-D electrode and one at the bottom. The bottom electrode was stainless steel shim (302 grade), 10 m wide and 51  $\mu\text{m}$  thick (SHM-302-0.051x203x300, Small Parts & Bearings Inc.) and was attached to the lower face of the bottom Terfenol-D element (i.e. Figure 4) using double sided copper tape  $\sim 100 \mu\text{m}$  thick. Wire with a diameter of 0.57 mm was used for the top electrode, and was attached to the side of the top Terfenol-D element using silver-loaded epoxy. After the epoxy was cured it was coated with silver ink (CW2200MTP, Circuitworks), this ensured that the top electrode made a low resistance ohmic-contact with the Terfenol-D. Care was taken to ensure that the epoxy did not interfere with the motion of the bearing on the upper surface of the top Terfenol-D element.

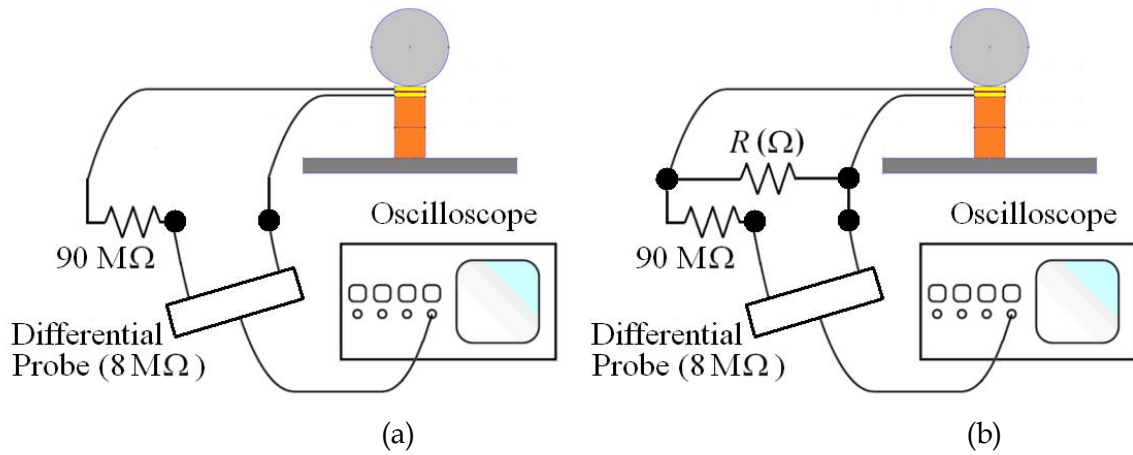


Figure 7. Experimental arrangements for the electrical measurements: (a) the circuit for measuring open circuit voltage, and (b) the circuit for sweeping load resistor  $R$ , and for load power measurements. (Originally published in reference [40]).

Two types of electrical measurements were made: (i) the ME transducer's open circuit voltage (Figure 7a), or (ii) the voltage across a linear resistive load that was attached across the transducer (Figure 7b). Voltage measurements were made using a 10:1 differential probe with 8 M $\Omega$  input impedance (Hameg HZ109), connected to a personal-computer based oscilloscope with one giga-sample memory (Picoscope 6403). Ring-down measurements of the harvester (discussed further in Section 4) were undertaken and suggested that the resonant frequency of the device was near 10 Hz. The measured capacitance of the ME transducer was 1.86 nF (see above), resulting in a capacitive reactance at 10 Hz of,

$$X_C = 1/(2 \pi f C) \sim 8.6 \text{ M}\Omega. \quad (6)$$

This reactance is larger than the input impedance of the differential probe that was used to measure the transducer voltage, and hence would have resulted in erroneous measured voltages (due to the voltage load-down effect of impedances in parallel). To obtain more accurate measured voltages it was decided to add 90 M $\Omega$  (i.e. nine 10 M $\Omega$  resistors) in series with the differential probe, as shown in Figure 7. To make allowance for the voltage divider effect (of adding the 90 M $\Omega$  in series with the probe) the ME transducer voltages that were subsequently measured were multiplied by  $d = (90 \text{ M}\Omega + 8 \text{ M}\Omega)/(8 \text{ M}\Omega) = 12.25$ . It was also determined that the differential probe was not correctly calibrated at low frequencies (i.e. near

DC). A 10 Hz output from a signal generator (50  $\Omega$  output impedance), set to a peak voltage of 2.04 V, was applied to the differential probe (set at 10:1). The probe subsequently measured a peak voltage of 1.64 V, indicating that a further voltage multiplication was required, being  $e = 2.04/1.64 \sim 1.244$ . The total voltage multiplier was therefore  $d \times e = 15.24$  (i.e. voltages measured by the differential probe were multiplied by this amount).

## 4. Results and Discussion

The discussion is divided into two main parts. The first part will present model predictions of the mechanical and magnetostatic behaviour of the harvester. Scaling laws will also be presented that allow predictions of the mechanical behaviour of similarly arranged harvesters with different geometric ratios. The second part will discuss the experimental measurements, both mechanical and electrical, that have been made to determine the performance of the bi-axial, magnetoelectric vibration energy harvester. In particular, a simple demonstrator has been built (see Figure 6a) and its behaviour elucidated.

### 4.1 Mechanical and magnetostatic predictions

#### 4.1.1 Restoring force predictions

Using the three-dimensional model described in Section 2.2 (and Appendix B) force predictions were made as the bearing was swept in the  $y$  -  $z$  plane (see Figure 5), with the origin located at the centre of the uppermost horizontal surface of the magnets.

Varying the bearing offset in the  $z$ -direction (i.e. the  $z$ -offset) can be thought of as varying the thickness of the ME transducer located between the bearing and the magnets. Figure 8a shows the variation of the predicted restoring force  $F_y$  acting on the bearing (in the  $y$ -direction) with increasing bearing offset in the  $y$ -direction for a constant  $z$ -offset. The restoring force  $F_y$  appears to be hookean in nature about the centre of the magnet. The spring constant (i.e. slope) varies from 1220 N/m for a  $z$ -offset of 0.5 mm (i.e. corresponding to a transducer 0.5 mm thick), to 260 N/m for a  $z$ -offset of 3.5 mm (i.e. corresponding to a transducer 3.5 mm thick). As the bearing approaches the edge of the magnet the restoring force  $|F_y|$  behaves like a softening-spring, as shown in Figure 8a.

Predictions of the magnetic attractive force  $|F_z|$  between the bearing and the magnet (in the  $z$ -direction) are shown in Figure 8b as a function of bearing offset in the  $y$ -direction (i.e.  $y$ -offset). As might be expected, the force increases rapidly as the bearing moves closer to the magnet (i.e. decreasing  $z$ -offset). For a constant  $z$ -offset, as the  $y$ -offset increases the force  $|F_z|$  decreases due to the cylindrical geometry of the magnet.

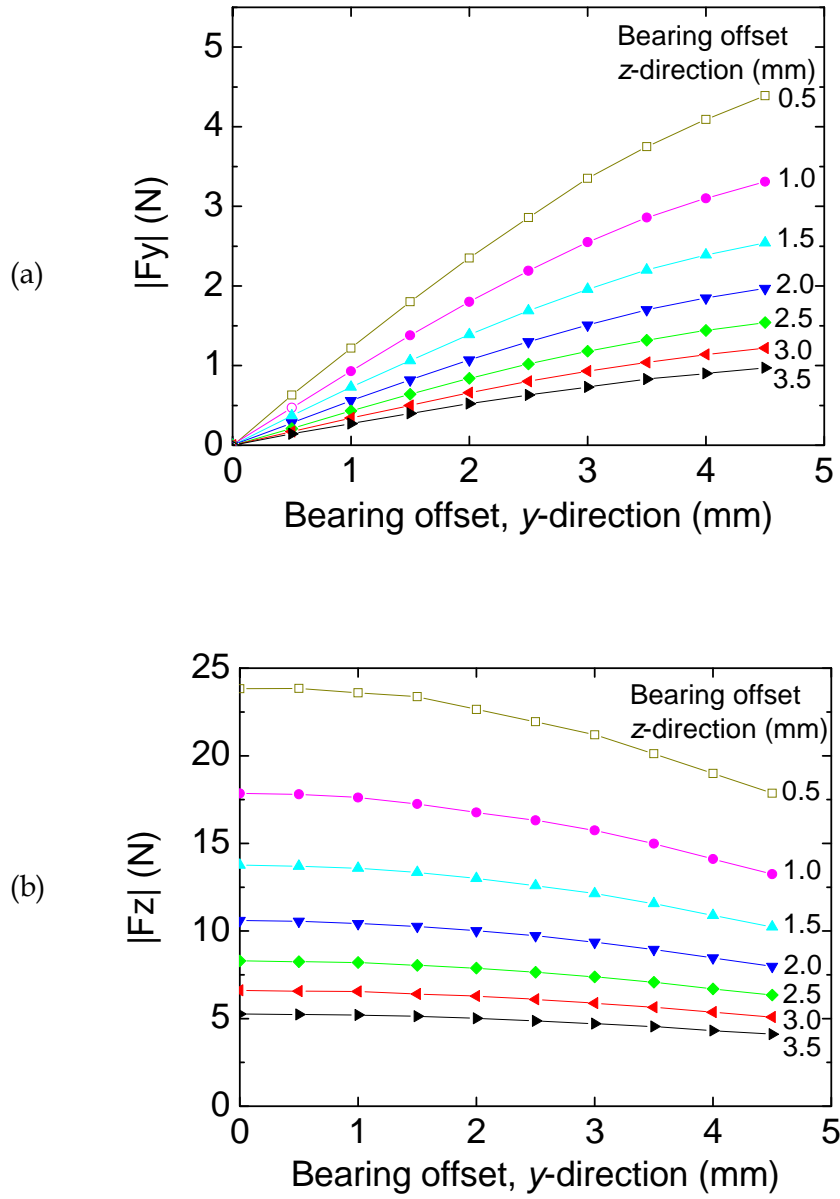


Figure 8. Force predictions showing (a)  $|F_y|$ , and (b)  $|F_z|$  as a function of bearing offset in both the y and z directions

For the demonstrated harvester (Figure 6a) the magnetic force predictions were made assuming that the 3.5 mm ME transducer acted as a 3.5 mm air gap between the magnet and the bearing. That case is represented by the black curves in Figure 8. Figure 8a predicts that  $F_y$  is linear near the central-line (i.e.  $y \leq 2.0$  mm) and has an effective spring constant of  $k = 260$  N/m. The bearing mass is approximately  $m = 67$  grams, and hence the predicted resonant frequency of the bearing/magnet arrangement is,

$$f_{\text{RESONANCE}} = (1/2\pi)\sqrt{k/m} \sim 9.9 \text{ Hz.}$$

#### 4.1.2 Magnetic field predictions

Comsol was also used to visualise the static magnetic field distribution for various bearing positions. Of particular interest is the distribution of magnetic flux density  $B$  in the ME transducer since this determines the stress distribution in the transducer, and hence the voltage generated. As described in Section 2.1 (and Appendix A) two-dimensional modelling of the Terfenol-D nonlinear magnetostrictive response was carried out using the approach described in reference [44]. Predicted magnetic flux distributions are shown in Figure 9, which magnifies the contact region between the bearing and the ME transducer. In Figure 9a the bearing is centred on the upper Terfenol-D element. When the ME transducer is first positioned at the top of the magnet a magnetostrictive 'shrinking' effect similar to that shown in Figure 2a is expected to occur, dictated by the arrangement of the streamlines. In Figure 9b the bearing is near the edge of the magnet (i.e. 4.5 mm from the central-line in the negative  $y$ -direction). The magnetic flux distribution in the upper Terfenol-D element changes significantly as the bearing changes position, as indicated by the change in the magnetic flux lines and the magnetic flux density colour contours (where red indicates high density and blue low density) in the upper Terfenol-D element. Again, it should be emphasised that the two-dimensional modelling should be considered qualitative due to the (necessary) approximation that the ME transducer, and also magnets, are uniformly 10 mm deep (i.e. cuboidal instead of cylindrical).

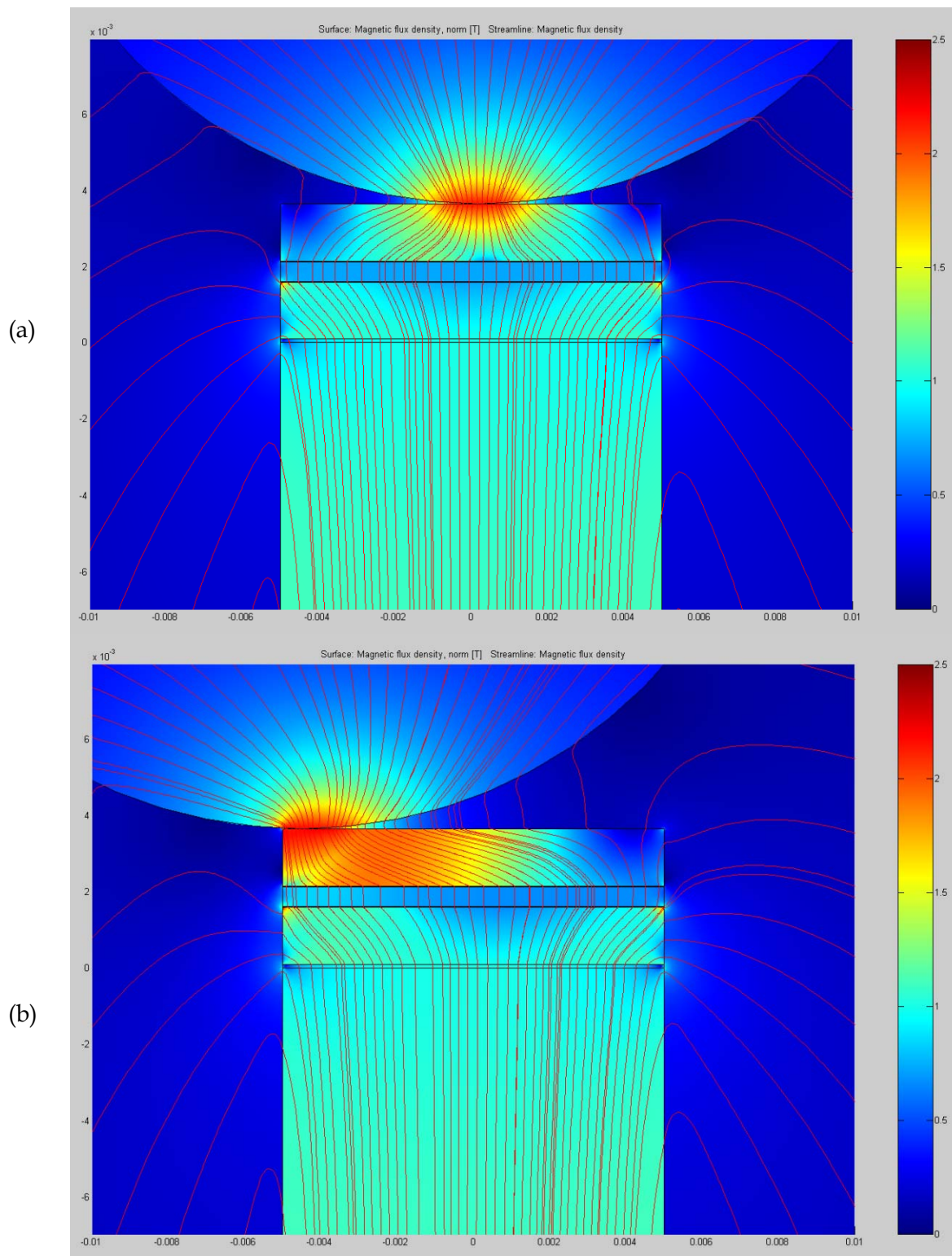


Figure 9. Predicted magnetic flux density and streamlines for (a) the bearing at the central rest position, and (b) the bearing near the edge of the ME transducer

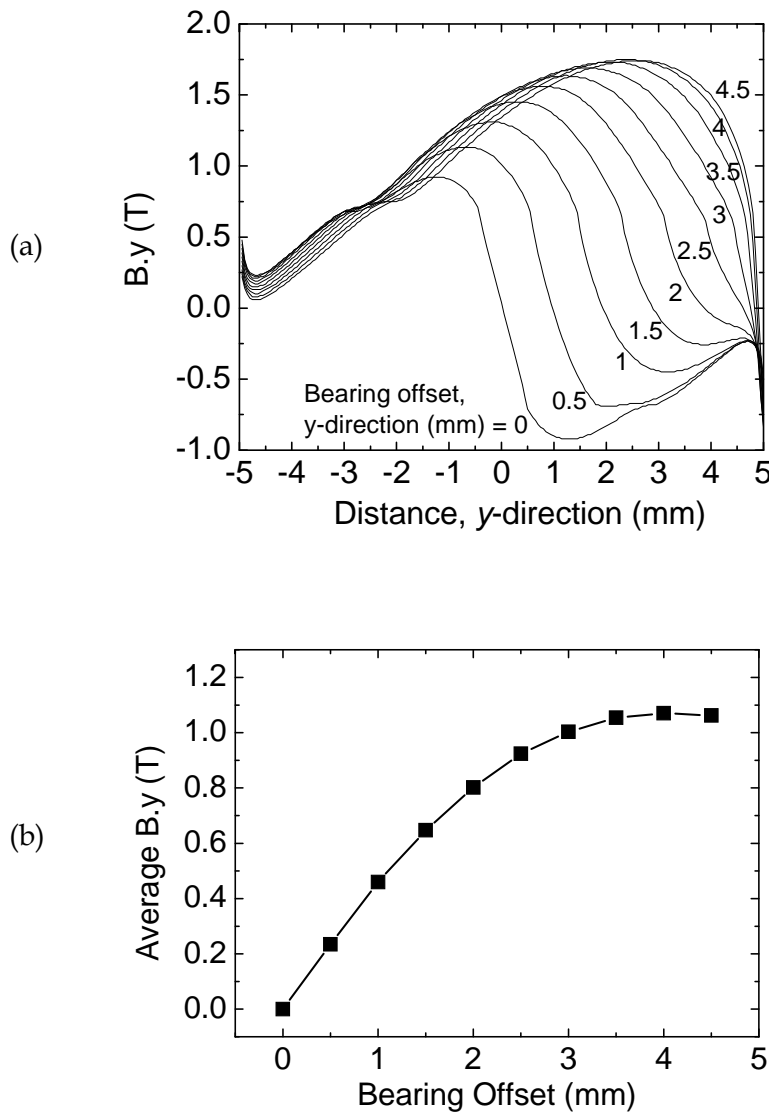


Figure 10. (a) Predicted magnetic flux density  $B$  in the  $y$ -direction (i.e.  $B.y$ ) as a function of distance along the lower edge of the upper magnetostrictive element.  $B.y$  is plotted as a function of bearing offset from the central-line, in the  $y$ -direction. The bearing offset is varied from zero (Figure 9a) to a maximum offset of 4.5 mm (Figure 9b). (b) Mean  $B.y$  as a function of bearing offset.

A closer examination of the predictions of the magnetic flux density  $B$ , in the  $y$ -direction, for the upper Terfenol-D element is presented in Figure 10. As the bearing moves across the surface of the upper Terfenol-D element (from the centre to the edge) Figure 10a shows that  $B.y$  changes direction. The bearing is steering the magnetic field through the ME transducer. Figure 10b presents the average of each  $B.y$  line plotted in Figure 10a. The large changes in both the magnitude and direction of the magnetic flux suggest that significant strain variations are being experienced at the piezoceramic layer.



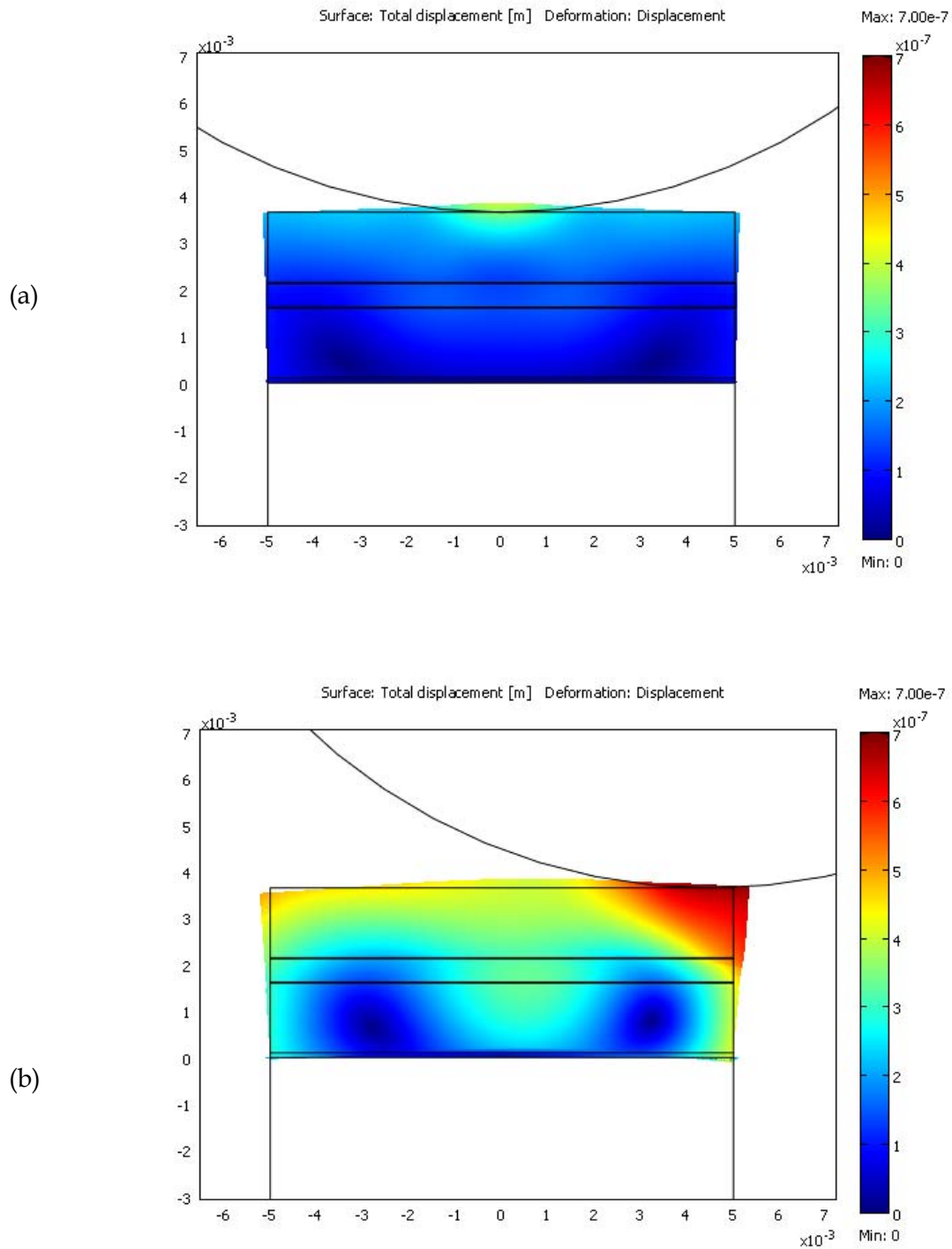


Figure 11. Predicted deformation of the ME transducer for (a) the bearing at the central rest position, and (b) the bearing near the edge of the ME transducer. Deformation has been amplified by a factor of 500.



As the bearing moves, the magnetic flux changes (shown in Figures 9 and 10) will induce deformation of the ME transducer via the magnetostrictive effect. Figure 11 shows the predicted two-dimensional deformation of the ME transducer, as the bearing location changes from the central rest position to near the edge of the transducer. The deformation process produces mechanical stress on the PZT element within the transducer, which may subsequently generate a piezoelectric voltage. As already mentioned, the deformations shown in Figure 11 are indicative only because of the geometric approximations in the two-dimensional modelling.

#### 4.1.3 Qualitative stress modelling

Shown in Figure 12 are qualitative predictions of the two-dimensional mechanical stress ( $y$ -direction) field in the ME transducer as the bearing location varies from the central rest position (Figure 12a) to near the edge of the ME transducer (Figure 12b). The predictions are qualitative only since they do not include any piezoelectric electromechanical effects and also assume a cuboid transducer geometry, however they may provide useful guidance for future three-dimensional predictions of stress distributions in the ME transducer. The measured sinusoidal open circuit piezoelectric voltage from the harvester (discussed in detail in Section 4.2) allows an estimate to be made of the mechanical stress in the PZT layer of the ME transducer. Knowing that the Pz27 disk used in the ME transducer had a thickness  $t_p = 0.5$  mm, with a piezoelectric voltage constant  $g_{31} = -0.0107$  Vm/N [51], and that the peak open circuit voltage was  $V_{OUT} \sim 45$  V (see Section 4.2, Figure 15), then by re-arranging equation (1) the stress difference in the PZT layer can be estimated as,

$$\Delta\sigma_{31p}^E = \left| \frac{V_{OUT}}{2 \times g_{31} \times t_p} \right| = \frac{45}{2 \times 0.0107 \times 0.5 \times 10^{-3}} = 4.2 \text{ MPa}. \quad (6)$$

Note that equation (6) relates to the stress variation in the PZT layer (in the  $y$ -direction), as the bearing moves from the central rest position to near the edge of the ME transducer (i.e. Figures 12a and 12b). However, the magnetic stream lines depicted in Figure 9 suggest that there is no bearing position (on the surface of the upper Terfenol-D element) that will produce a mechanical stress distribution in the ME transducer that is purely aligned with the  $y$ -direction, so the stress difference estimated by equation (6) will only be approximate. The stress difference estimated using equation (6) can be compared with the predicted stresses shown in Figure 12. Given that the average tensile stress in the piezoelectric element can be found by integrating the stress in the layer, then from Figure 12a with the bearing located at the central rest position, the average stress ( $y$ -direction) in the piezoelectric element is,

$$\sigma_{REST} = 6.15 \text{ N} / (10 \times 10^{-3} \times 0.5 \times 10^{-3}) = 1.23 \text{ MPa}.$$

From Figure 12b with the bearing located at the edge, the average tensile stress ( $y$ -direction) in the piezoelectric layer was,

$$\sigma_{EDGE} = 16.15 \text{ N} / (10 \times 10^{-3} \times 0.5 \times 10^{-3}) = 3.23 \text{ MPa}.$$

The stress difference in the piezoelectric layer as the bearing moves from the centre to the edge is then  $\sigma_{REST} - \sigma_{EDGE} = 2.0$  MPa, or about half the stress estimated using equation (6) which is reasonable considering the qualitative nature of the calculation. Note that the predicted stress in the piezoelectric layer, in the  $z$ -direction, was negligible for both bearing locations.

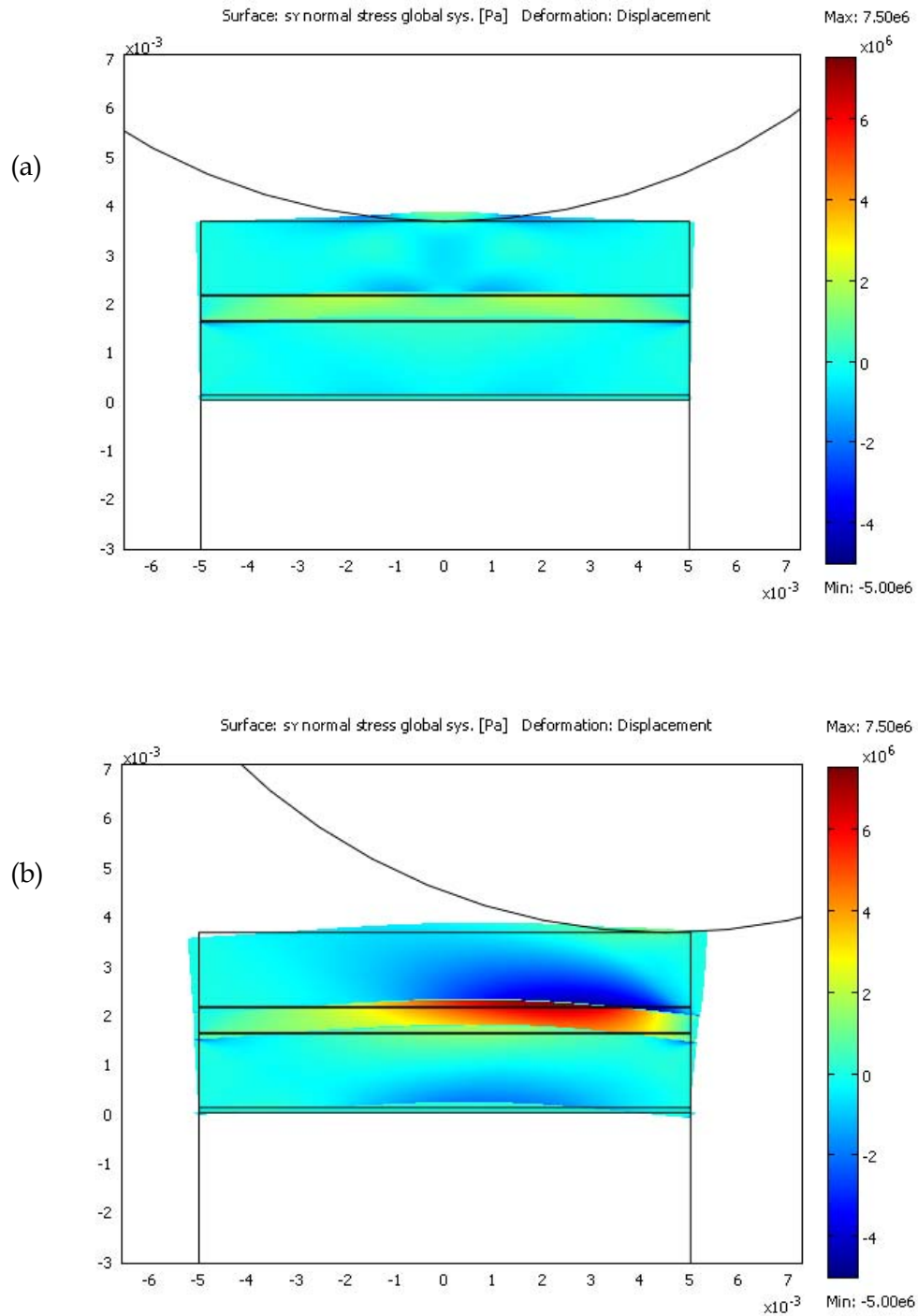


Figure 12. Qualitative two-dimensional stress (y-direction) in the ME transducer for (a) the bearing at the central rest position, and (b) the bearing near the edge of the ME transducer [i.e. 4.5 mm from the central-line]

#### 4.1.4 Scaling laws for the bi-axial vibration energy harvester

For the harvester arrangement shown in Figure 4, the rest position for the bearing is directly above the centre of the magnet (i.e. along the central-line). This is not always the case since it has been observed that a small diameter bearing sitting on the face of a large diameter cylindrical magnet may have a rest position away from the central-line of the magnet. From observation, it is hypothesised that for generic magnet and bearing diameters,  $D_{\text{MAGNET}}$  and  $D_{\text{BEARING}}$ , the bearing rest position will remain at the central-line as long as  $D_{\text{MAGNET}} \leq D_{\text{BEARING}}$ . For a given ratio  $D_{\text{MAGNET}}/D_{\text{BEARING}}$  (subject to the proviso that  $D_{\text{MAGNET}} \leq D_{\text{BEARING}}$ ) the scaling laws that apply are:

- (i)  $F_{\text{RESTORING}} \propto (D_{\text{BEARING}})^2$ ,
- (ii)  $k \propto D_{\text{BEARING}}$ ,
- (iii)  $f_{\text{RESONANCE}} \propto 1/D_{\text{BEARING}}$ .

Furthermore, for a lamina composite of thickness  $t$  (and all else being equal),

- (iv)  $k \propto 1/t$ .

## 4.2 Electro-mechanical measurements

### 4.2.1 Impedance as a function of frequency

The impedance of a PZT disk with diameter 10 mm and thickness 0.5 mm, was measured as a function of frequency both before and after bonding into a lamina composite arrangement (as described in Section 3). Figure 13a shows an extended frequency range, and Figure 13b magnifies the region near the resonant peaks A and B. As seen previously [11] after bonding of the PZT disk there is a substantial reduction of the resonant peaks compared with those of a free disk. Equation (6) and the impedances shown in Figure 13 can be used to estimate the capacitance of the PZT disk; prior to bonding its capacitance was 2.26 nF, and after bonding 1.86 nF.

To confirm that the 90 M $\Omega$  resistor chain described in Section 3 (and depicted in Figure 7) was suitable for use in measuring the voltage from the ME transducer, its impedance was measured as a function of frequency. Figure 14 shows that the 90 M $\Omega$  resistor chain's impedance is constant from 1 Hz to 110 Hz (with a small glitch at the 50 Hz mains frequency), after which the impedance begins to roll-off, presumably due to electrical self-resonance. Since the harvester's mechanical resonance occurs at 10 Hz, the 110 Hz roll-off was deemed sufficiently high so as to not interfere with the measurement of transducer voltage.

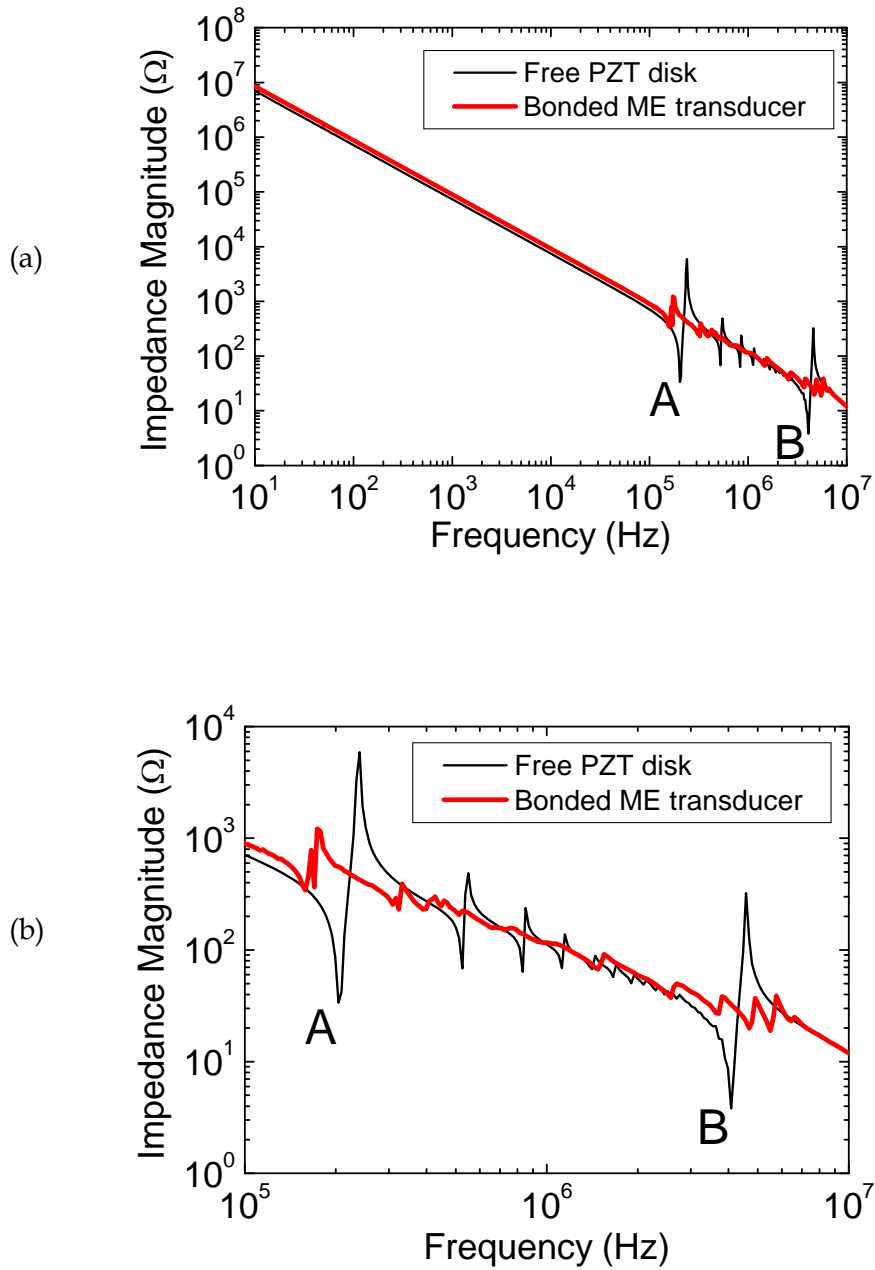


Figure 13. Measured impedance magnitude of a free PZT disk with diameter 10 mm and thickness 0.5 mm, and of the disk when bonded into a ME transducer arrangement as described in Section 3. For the free disk, the fundamental lateral and thickness resonant frequencies are labelled A and B respectively. Shown in (a) is the measured impedance over an extended frequency range, and in (b) a magnification of the frequency range near the resonant peaks.

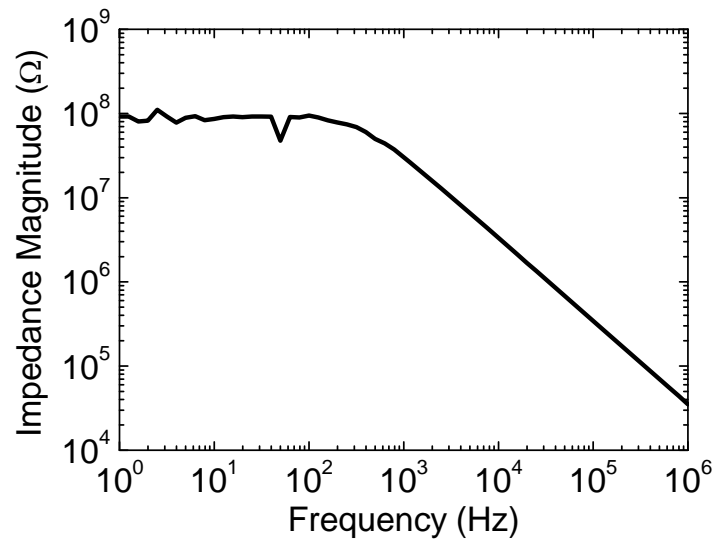


Figure 14. Measured impedance of the 90 MΩ resistor chain (shown in Figure 7)

#### 4.2.2 Magnetoelectric voltage and bearing displacements as a function of frequency and drive angle

The bi-axial nature of the energy harvester is clearly seen in Figures 15a and 15b. Figure 15a is a graph showing nineteen measured frequency sweeps of the peak open circuit voltage generated by the harvester. Sweeps were measured from low to high frequency, in 0.2 Hz steps. A maximum rms host acceleration of 61 mG was chosen because, at resonance, larger host accelerations would drive the bearing off the ME transducer. A laser displacement sensor was used to measure the bearing displacement ( $y$ -direction) during testing. The host acceleration was uni-axial in the  $y$ -direction. After each sweep the harvester was rotated by 5 degrees (about the harvester's central-line) from the initial position, designated as angle 0°, through to an angle of 90°. For each sweep the bearing's resonant response occurred at 9.8 Hz, similar to predicted value stated previously. Figure 15b shows the maximum measured peak open circuit voltage and displacement as a function of angle (for each of the sweeps shown in Figure 15a), and it can be seen that the harvester generates  $\sim 9$  V per millimeter of bearing displacement.

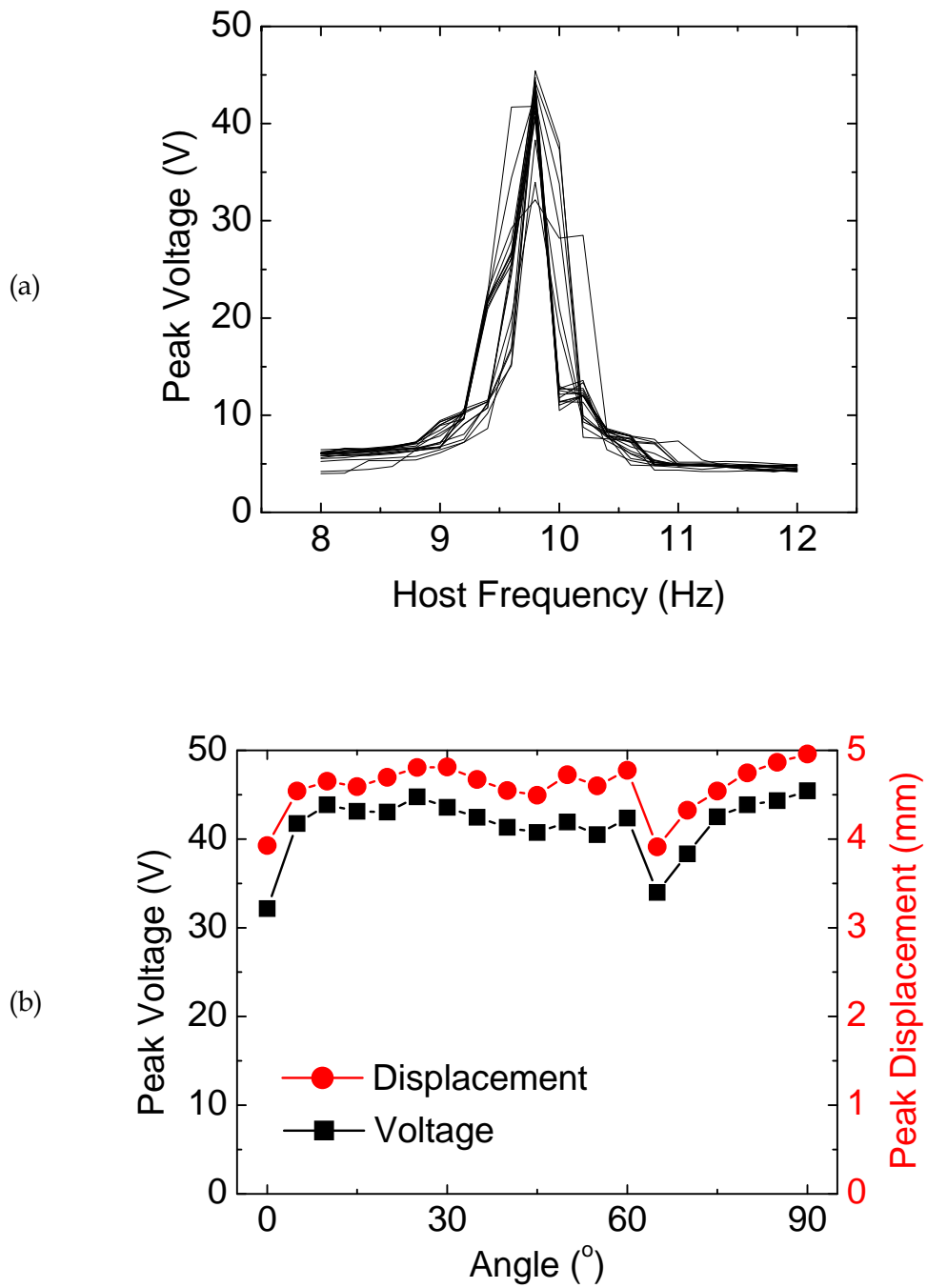


Figure 15. (a) Harvester peak open circuit voltage measured as a function of drive frequency, and (b) the measured peak voltage and displacement of the bearing (at resonance) as a function of drive angle. (Originally published in reference [40]).

### 4.2.3 Magnetolectric voltage as a function of host acceleration

The peak open circuit voltage of the harvester, and the peak displacement of the bearing, were measured (at resonance) as a function of rms host acceleration. As the rms host acceleration was varied, the resonant frequency did not significantly change. Figure 16 shows that below an rms host acceleration of 40 mG the measured open circuit voltages (and bearing displacements) increased in an approximately linear fashion. There is however a clear gradient increase for both displacement and voltage when the rms host acceleration is larger than  $\sim 40$  mG. It is surmised that the behavior shown in Figure 16 is due to the softening-spring effect (as described previously, Figure 8a). It is worth noting that the harvester generates  $\sim 9$  V per millimeter of bearing displacement, independent of the absolute value of the bearing displacement.

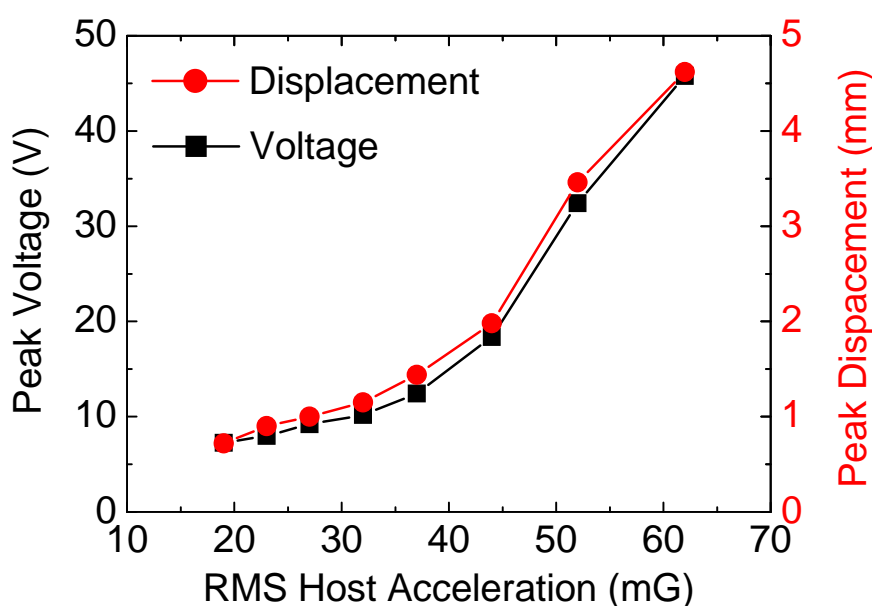


Figure 16. Measured peak open circuit voltage, and bearing peak displacement (at resonance), as a function of rms host acceleration. (Originally published in reference [40]).

### 4.2.4 Harvester output power as a function of load resistance

A sweep through a range of load resistor values was carried out to determine the rms output power of the harvester. Using an rms host acceleration of 61 mG at 9.8 Hz, the measured peak load voltage was 23.9 V across a  $3.3 \text{ M}\Omega$  load resistor yielding a maximum rms load power of  $121 \text{ }\mu\text{W}$  (Figure 17). At the maximum load power, the measured peak bearing displacement was 4.61 mm, hence the peak kinetic energy of the 67 gram bearing is estimated to be 2.7 mJ.

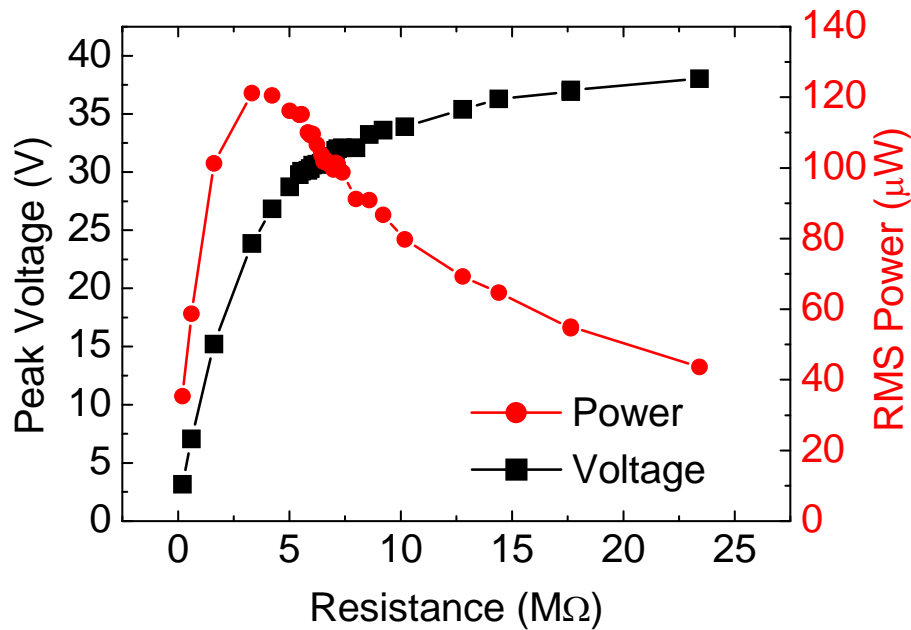


Figure 17. Measured maximum peak voltage, and rms power, as a function of load resistance. (Originally published in reference [40]).

### 4.3 Future work

The modelling of the bi-axial energy harvester, and laboratory demonstration of the harvesting concept, both described in this report have provided valuable lessons to assist with the development of the next generation of harvester. An artist's impression of and assembled harvester was shown in Figure 3. The effects of adding a cylindrical 'bearing housing' to constrain the bearing's movement and also to introduce a vibro-impact effect [9] will need to be examined. Rotational effects produced by the bearing rolling across the surface of the Terfenol-D were ignored in this report, and will need to be examined in future work. For example the rotational effects may prove important in addressing surface wear at the bearing/Terfenol-D interface which has been found to be an issue. The modelling presented in this report is preliminary. Of particular importance is the inclusion of piezoelectric (i.e. electromechanical) effects in the models, which will require the use of the Comsol piezoelectric application mode. This will allow examination of the electric fields in the piezoelectric layer, and hence allow predictions to be made of the magnetoelectric voltages being generated by the ME transducer. The modelling of the Terfenol-D layers will need to be more complex to address the magnetostrictive response at low applied magnetic field levels, in particular for the situation  $I/I_s \leq 1/\sqrt{3}$  in equation (4). Reference [44] adopts a magnetostriction constant of  $\lambda_s = 2 \times 10^{-4}$ , the validity of this choice of  $\lambda_s$  [used in equation (4)] will be further examined. To fully understand the bi-axial harvesters operation the three-dimensional stress (and strain) distribution within the ME transducer needs to be examined as



a function of bearing position. Eddy current losses need to be quantified, although they are expected to be small due to the low frequency nature of the bi-axial harvester. Finally, the response of the bi-axial harvester to a bi-axial excitation needs to be examined.

## 5. Conclusion

DSTO is investigating vibration energy harvesting approaches with the ultimate goal of capturing airframe vibrational energy, and then converting it into electrical power for use by structural health monitoring sensors and devices. This report investigated a bi-axial vibration energy harvesting approach with the aim of harvesting energy from the multi-axis accelerations that can be experienced by an aircraft. A bi-axial oscillator was created using a permanent-magnet/ball-bearing arrangement. The magnet produces a bi-axial restoring force on the bearing, and as the bearing oscillates it steers magnetic field through a magnetostrictive/piezoelectric laminate transducer thereby producing an oscillating charge that can be harvested. The chosen harvester arrangement consisted of a steel ball-bearing with 25.4 mm diameter, and a rare-earth magnet and magnetoelectric (ME) transducer both with 10 mm diameter. Modelling indicated that the magnetic restoring force has an effective spring constant of 260 N/m when the ME transducer 3.5 mm thick. Modelling was also used to make a qualitative assessment of the magnetic flux changes in the ME transducer as the bearing oscillates, which indicated that large flux variations occur as the bearing moves from the magnets central-line towards the edge. A simple laboratory demonstrator of a bi-axial ME energy harvester was created using a Terfenol-D/lead zirconate titanate/Terfenol-D transducer. Harvester output was measured as a function of drive-angle, host acceleration, and load resistance. The harvester produced a peak rms power of 121  $\mu$ W from an rms host acceleration of 61 mG at 9.8 Hz.

## 6. Acknowledgement

The authors would like to acknowledge the help of Steve Lamb for his assistance in the machining of the Terfenol-D specimens.

## 7. References

1. S. Galea, S. van der Velden, S. Moss, I. Powlesland, "On the Way to Autonomy: the Wireless-interrogated and Self-powered 'Smart Patch' System," in "Encyclopedia of Structural Health Monitoring," Editors-in-Chief: C. Boller, F. K. Chang and Y. Fujino, Chpt. 76, John Wiley & Sons, ISBN 978-0-470-05822-0, 2009.
2. S. Galea, T. Trueman, L. Davidson, P. Trathen, B. Hinton, A. Wilson, T. Muster, I. Cole, P. Corrigan and D. Price, "Aircraft Structural Diagnostic and Prognostic Health Monitoring for Corrosion Prevention and Control" in "Encyclopedia of Structural Health Monitoring," Editors-in-Chief: C. Boller, F. K. Chang and Y. Fujino, Chpt. 112, John Wiley & Sons, ISBN 978-0-470-05822-0, 2009.
3. S. C. Warren-Smith, H. Ebendorff-Heidepriem, T. C. Foo, R. Moore, C. Davis, T. M. Monro, "Exposed-core Microstructured Optical Fibers for Real-time Fluorescence Sensing," *Optics Express*, Vol. 17, No. 21, pp. 18533-18542, 2009.
4. N. Rajic, "Development of an Active Smart Patch for Aircraft Repair," in "Encyclopedia of Structural Health Monitoring," Editors-in-Chief: C. Boller, F. K. Chang and Y. Fujino, Chpt. 107, John Wiley & Sons, ISBN 978-0-470-05822-0, 2009.
5. S. Galea and I. Powlesland, "Caribou Loads Flight Survey Using A Rapid Operational Loads Measurement Approach", *Materials Forum*, Vol. 33, p. 100, 2009.
6. S. Moss, I. Powlesland, S. Galea, G. Carman, "Vibro-impacting Power Harvester," *Proc. SPIE*, Vol. 7643, 76431A, 2010.
7. S. Moss, I. Powlesland, M. Konak, A. Barry, S. Galea, and G. Carman, "Broad-Band Vibro-Impacting Energy Harvester," *Mat. Sci. Forum*, Vols. 654-656, p. 2799, 2010.
8. S. Moss, A. Barry, I. Powlesland, S. Galea, G. P. Carman, "A low Profile Vibro-impacting Power Harvester with Symmetrical Stops," *App. Phys. Lett.*, Vol. 97, p. 234101, 2010.
9. S. Moss, A. Barry, I. Powlesland, S. Galea, G. P. Carman, "A broad-band Vibro-impacting Power Harvester with Symmetrical Piezoelectric Bimorph-stops," *Smart Mater. Struct.*, Vol. 20, p. 045013, 2011.
10. S. Moss, P. McMahon, M. Konak, C. Phoumsavanh, N. Rajic, S. Galea, I. Powlesland, "Modelling and Experimental Validations of the Acoustic Electric Feedthrough Technique," DSTO-RR-0338, 2008.
11. S. Moss, M. Konak, C. Phoumsavanh, K. Tsoi, I. Powlesland, "Acoustic Electric Feedthrough Demonstrator Mk-I," DSTO-TR-2296, 2009.

12. S. Moss, C. Phoumsavanh, M. Konak, K. Tsoi, N. Rajic, S. Galea, I. Powlesland, P. McMahon, "Design of the Acoustic Electric Feedthrough Demonstrator Mk-II," *Mat. Forum*, Vol. 33, p. 187, 2009.
13. S. Moss, J. Skippen, M. Konak, I. Powlesland, "Footprint Reduction for the Acoustic Electric Feedthrough Technique," DSTO-TR-2395, 2010.
14. S. Moss, J. Skippen, M. Konak, I. Powlesland, and S. Galea, "Detachable Acoustic Electric Feedthrough," *Proc. SPIE* 7647, p. 764745, 2010.
15. J. P. Joule, "On the Effects of Magnetism upon the Dimensions of Iron and Steel Bars," *The London, Edinburgh and Dublin Philosophical Magazine and Journal of Science* (Taylor & Francis), Third Series, pp. 76-87, 1847. Retrieved from Google books, 29<sup>th</sup> May 2011:  
<http://books.google.com/books?id=VEgEAAAAAYAAJ&lpg=PA76&dq=joule+annals+electricity+219+1842&pg=PA76&hl=en#v=onepage&q=joule%20annals%20electricity%20219%201842&f=false>
16. R. C. Smith, "Smart Material Systems Model Development," Siam, Philadelphia, ISBN 0-89871-583-0, 2005.
17. G. Engdahl, "Handbook of Giant Magnetostrictive Materials," Academic, New York, ISBN 978-0-12-238640-4, 2000.
18. P. Curie, J. Curie, "Développement par Pression de l'électricité Polaire dans les Cristaux Hémihédres à Faces Inclinées", *Bulletin de la Société Minéralogique de France*, Vol. 3, p. 90. 1880 and C. R. Acad. Sc. Paris, Vol. 91, p. 294, 1880.
19. G. Lippman, " Principe de la Conservation de L'électricité, ou Second Principe de la Théorie des Phénomènes Électriques", *Annales de Chimie et de Physique*, Vol. 24, p. 145, 1881.
20. G. Shirane, E. Sawaguchi, Y. Takagi, "Dielectric Properties of Lead Zirconate," *Phys. Rev.*, Vol. 84, p. 476, 1951.
21. M. Fiebig, "Revival of the Magnetoelectric Effect," *J. Phys. D: App. Phys*, Vol. 38, p. R123, 2005.
22. P. Debye, "Bemerkung zu Einigen neuen Versuchen über Einen Magneto-elektrischen Richteffekt," *Z. Phys.*, Vol. 36, p. 300, 1926.
23. W. C. Rontgen, "Ueber die durch Bewegung eines im Homogenen Electricischen Felde befindlichen Dielectricums Hervorgerufene Electrodynamische Kraft," *Ann. Phys. Chem.*, Vol. 35, p. 264, 1888.
24. P. Curie, "Sur la symétrie dans les Phénomènes Physiques, Symétrie d'un Champ Électrique et d'un Champ Magnétique," *J. Physique*, Vol. 3, p. 393, 1894.

25. J. Ryu, A. V. Carazo, K. Uchino, H. E. Kim, "Magnetoelectric Properties in Piezoelectric and Magnetostrictive Laminate Composites", *Jpn. J. Appl. Phys.*, Vol. 40, p. 4948, 2001.
26. Ed. C. Piguet, "Low-Power Electronics Design," CRC Press, Florida, ISBN 0-8493-1941-2, 2005.
27. Eds. S. Priya, and D. J. Inman, "Energy Harvesting Technologies," Springer, New York, ISBN 978-0-387-76464-1, 2009.
28. S. Beeby (Editor), N. White (Editor), "Energy Harvesting for Autonomous Systems (Smart Materials, Structures, and Systems)," Artech House, ISBN 9781596937185, 2010.
29. S. Roundy, "On the Effectiveness of Vibration Based Energy Harvesting," *J. Int. Mat. Sys. Struct.*, Vol. 16, p. 809, 2005.
30. S Adhikari, M. I. Friswell, and D. J. Inman, "Piezoelectric Energy Harvesting from Broadband Random Vibrations," *Smart Mater. Struct.*, Vol. 20, p. 045013, 2011.
31. S. R. Anton, H. A. Sodano, "A review of Power Harvesting using Piezoelectric Materials (2003-2006)," *Smart Mater. Struct.*, Vol. 16, p. R1, 2007.
32. D. P. Arnold, "Review of Microscale Magnetic Power Generation," *IEEE Trans. Mag.*, Vol. 43, p. 3940, 2007.
33. H. Kim, W. Lee, H. V. Rasika Dias, and S. Priya, "Piezoelectric Microgenerators – Current Status and Challenges," *IEEE Trans. Ultra. Ferro. Freq. Cont.*, Vol. 56, p. 1555, 2009.
34. A. Erturk and D. J. Inman, "'Issues in Mathematical Modelling of Piezoelectric Energy Harvesters'," *Smart Mater. Struct.*, Vol. 17, p. 065016, 2008.
35. S. Roundy, P. K. Wright, and J. M. Rabaey, "Energy Scavenging for Wireless Sensor Networks with Special Focus on Vibrations," Kluwer- Academic, Massachusetts, ISBN 1402076630, 2004.
36. S. P. Beeby, R.N. Torah, M. J. Tudor, P. Glynn-Jones, T. O'Donnell, C.R. Saha, and S. Roy, "A Micro Electromagnetic Generator for Vibration Energy Harvesting," *J. Micromech. Microeng.*, Vol. 17, p. 1257, 2007.
37. N. Nersessian, S. W. Or, and G. P. Carman, "Magnetoelectric Behaviour of Terfenol-D Composite and Lead Zirconate Titanate Ceramic Laminates," *IEEE Trans. Mag.*, Vol. 40, p. 2646, 2004.
38. J. Ma, J. Hu, Z. Li, and C. Nan, "Recent Progress in Multiferroic Magnetoelectric Composites: from Bulk to Thin Films," *Adv. Mater.*, Vol. 23, p. 1062, 2011.

39. X. Dai, Y. Wen, P. Li, J. Yang, and M. Li, "A Micro Electromagnetic Generator for Vibration Energy Harvesting," *Sens. Act. A: Phys.*, Vol. 166, p. 94, 2011.
40. S. D. Moss, J. E. McLeod, I. G. Powlesland, S. C. Galea, "A Bi-axial Magnetoelectric Vibration Energy Harvester," *Sens. Actuators A: Phys.*, Vol. 175, p. 165, 2011.
41. S. Moss, U.S. provisional patent application number 61/482,496 "Vibration Energy Conversion Device," priority date 4<sup>th</sup> May, 2011.
42. COMSOL AB, COMSOL Multiphysics User's Guide, Version 3.5a, 2008.
43. COMSOL AB, AC/DC Module Users Guide, Version 3.5a, 2008.
44. <http://www.comsol.com/showroom/documentation/model/6063/>
45. E. W. Lee, "Magnetostriction and Magnetomechanical Effects," *Rep. Prog. Phys.*, Vol. 18, p. 184, 1955.
46. S. Chikazumi, "Physics of Ferromagnetism (2<sup>nd</sup> edition)," Oxford University Press, New York, ISBN 0-19-851776-9, 1997.
47. N. Rajic, "A Numerical Model for the Piezoelectric Transduction of Stress Waves," *Smart Mater. Struct.*, Vol. 15, p.1151, 2006.
48. Mathworks, Matlab 2007b.
49. M. A. Heald, J. B Marion, "Classical Electromagnetic Radiation (3<sup>rd</sup> edition)," Saunders, USA, ISBN 0-03-097277-9, 1995.
50. J. Morgan, S. Townley, G. Kemble, and R. Smith, "Measurement of Physical and Mechanical Properties of Beeswax," *Mat. Sci. and Tech.*, Vol. 18, p. 463, 2002.
51. Material Data Matrix, Ferroperm Piezoceramics A/S, [www.ferroperm-piezo.com](http://www.ferroperm-piezo.com) , April 2011.

## Appendix A: Two-dimensional Modelling

This appendix provides detailed instructions on using Comsol multi-physics software [42] to carry out two-dimensional modelling of the bi-axial magnetoelectric vibration energy harvester described in this report. Two-dimensional modelling of the harvester's magnetostrictive (Terfenol-D) elements follows the approach outlined in reference [44].

### MODEL NAVIGATOR

1. Start COMSOL Multiphysics software.
2. Under **Space Dimension**, choose 2D (see Figure A1).
3. In the application mode list, open **AC/DC Module>Statics, Magnetic>Perpendicular Induction Currents, Vector Potential**.
4. Click the **Multiphysics** button and then the **Add** button.
5. In the application mode list, open **Structural Mechanics Module>Plane Strain**.
6. Click the **Add** button.
7. Click **OK** to close the **Model Navigator**.

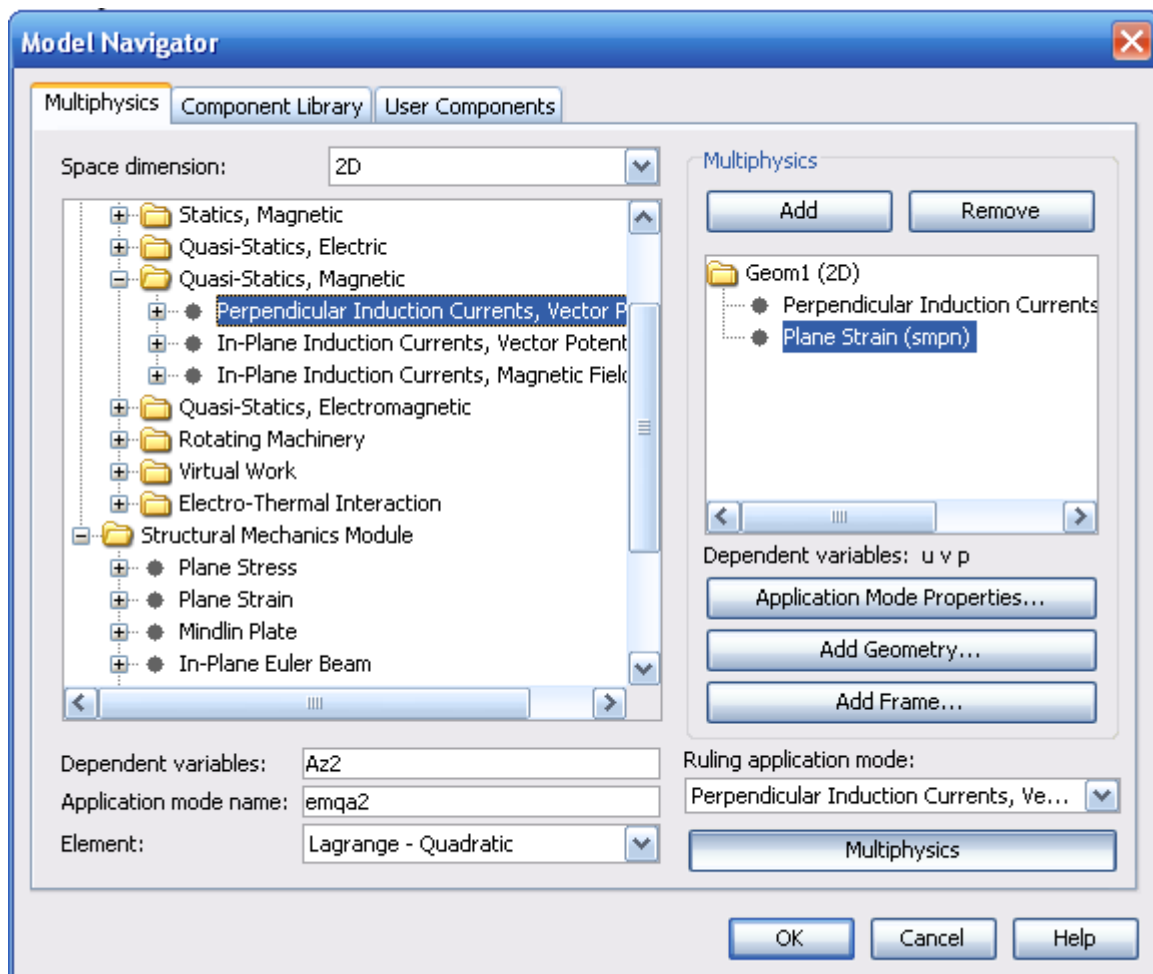


Figure A1. Comsol model navigator

**GEOMETRY MODELLING**

1. Shift-click the **Rectangle/Square** button on the Draw toolbar for each shape, and enter the parameters given in Table A1 (the description is only for the readers information).

Table A1. *Geometric settings for the harvester model*

Size		Position		
Width	Height	X	Y	(Description)
0.3	0.2	-0.15	-0.1	Air
0.07	0.005	-0.035	-0.029	Base Plate
0.01	0.012	-0.005	-0.024	Lower Magnet
0.01	0.012	-0.005	-0.012	Upper Magnet
0.01	1.0E-4	-0.005	0	Bond
0.01	0.0015	-0.005	1.0E-4	Lower Terfenol-D layer
0.01	2.5E-5	-0.005	0.0016	Bond
0.01	5.0E-4	-0.005	0.001625	PZT layer
0.01	2.5E-5	-0.005	0.002125	Bond
0.01	0.0015	-0.005	0.00215	Upper Terfenol-D layer

2. Shift-click the **Ellipse/Circle (Centred)** button.
3. In the **Circle** dialog box, type *0.0127* in the **Radius** edit field and set the centre coordinates to (0, 0.1635) by typing *0* in the **X** edit field and *0.01635* in the **Y** edit field (this is the ball bearing).
4. Click the **Point** button on the Draw toolbar, and draw a point at (0, 0). The completed geometry should look similar to that shown in Figure A2.

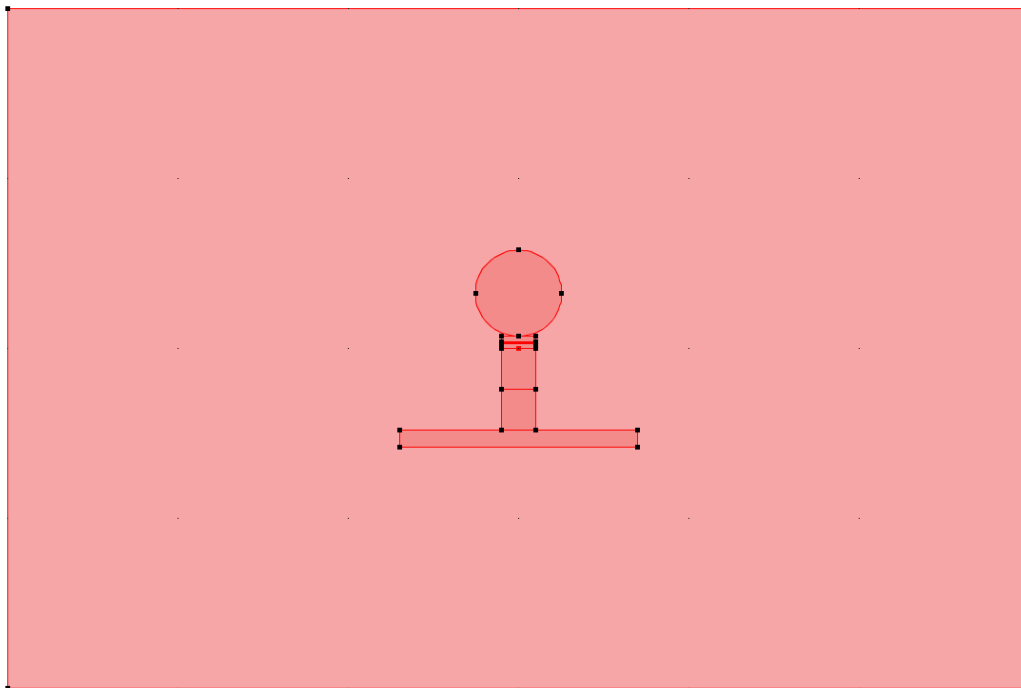


Figure A2. *Comsol geometry modelling*

**OPTIONS**

1. From the **Options** menu, open the **Constants** dialog box (see Figure A3).
2. Enter a constant with the name *Lambda\_s*, the expression *200E-6*, and the description *magnetostriction constant* (the description is optional).
3. Enter a constant with the name *Msat*, the expression *1500E3[A/m]*, and the description *saturation magnetisation* (the description is optional).
4. Click **Apply** and **OK** to close the **Constants** dialog box.

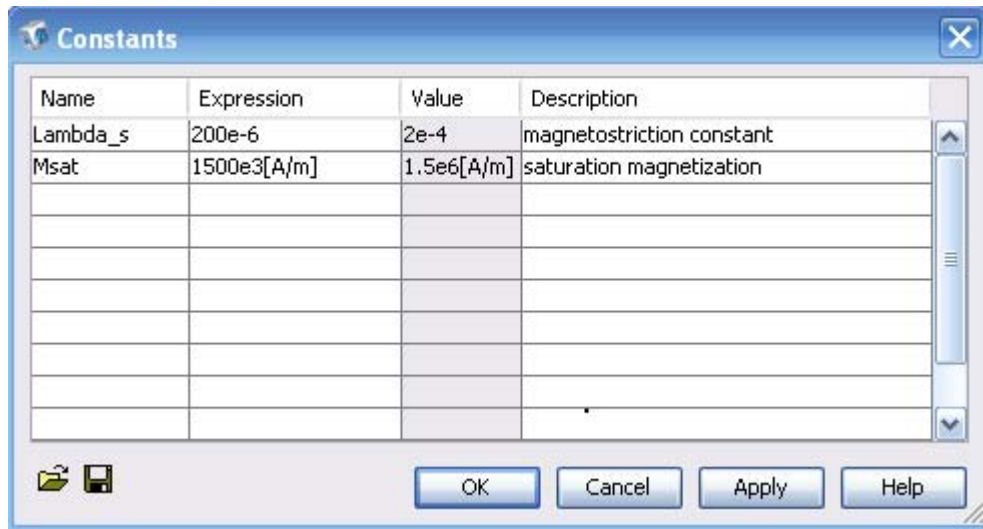


Figure A3. Comsol constants dialog box

5. From the **Options** menu, open the **Functions** dialog box.
6. Click the **New** button.
7. In the **Function Name** field, enter **HBFe**.
8. Select the **Interpolation** tick box, and select **File** in the list to **Use data from**.
9. Locate the data file required, or alternatively enter the data as a table (the multimedia accompaniment to this report contains the file 'HBFe.txt', also see Figure A4).
10. Select **Linear** in the **Interpolation method** list.
11. Click **Apply** and **OK** to close the **Functions** dialog box.



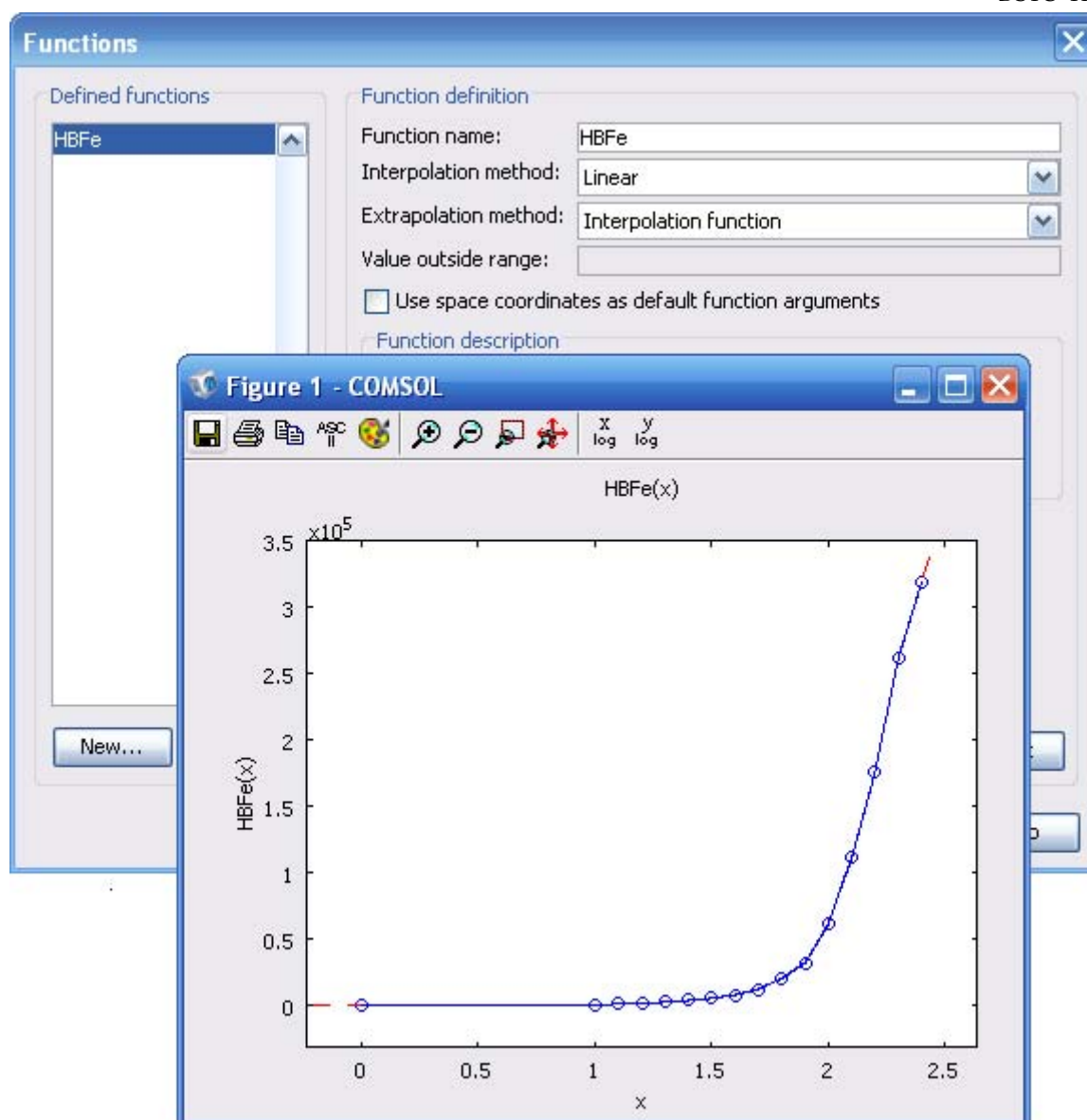


Figure A4. Comsol functions dialog box

12. From the **Options** menu, under **Expressions**, select **Subdomain Expressions**.
13. Select subdomains 6 and 10, and an expression with the name  $\text{Lambda}_x$ , and the expression  $1.5 \cdot \text{Lambda}_s \cdot (\text{Mx\_emqa} / \text{Msat})^2$ . (See Figure A5).
14. Then enter another expression with the name  $\text{Lambda}_y$ , and the expression  $1.5 \cdot \text{Lambda}_s \cdot (\text{My\_emqa} / \text{Msat})^2$ .

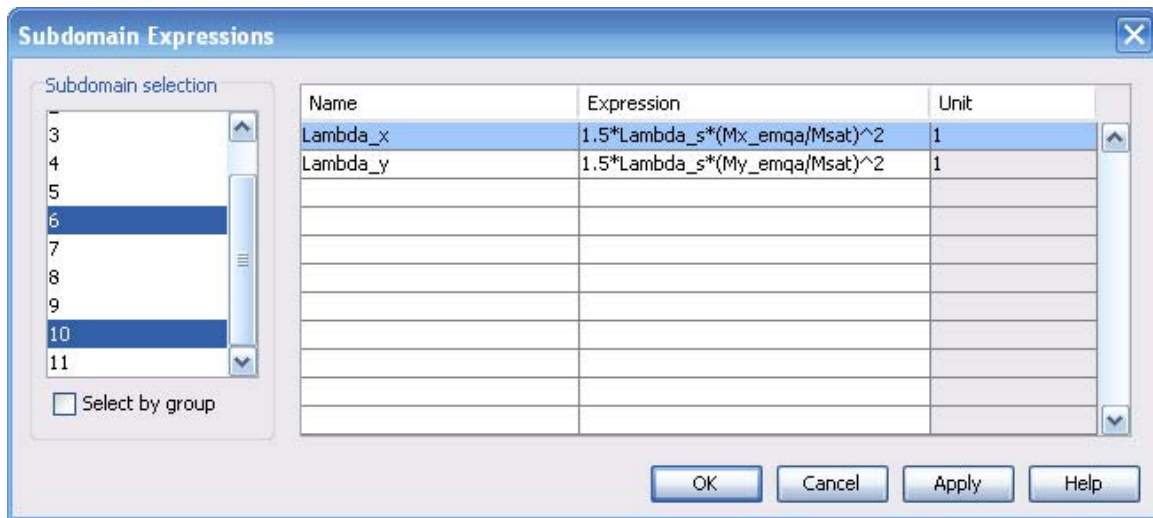


Figure A5. Comsol subdomain expressions dialog box

## PHYSICS SETTINGS

### *Subdomain Settings - Perpendicular Induction Currents, Vector Potential*

1. From the **Multiphysics** menu, select the **Conductive Media DC** application mode (see Figure A6).
2. From the **Physics** menu, select **Subdomain Settings**.
3. In the **Subdomain Settings** dialog box, select each subdomain and enter the parameters given in Table A2.

Table A2. Subdomain settings for the harvester model

Subdomains	Library Material	L	$\mathbf{H} \leftrightarrow \mathbf{B}$	Other
1, 5, 7, 8, 9	NA	0.01	$\mathbf{B} = \mu_0 \mu_r \mathbf{H}$	$\mu_r = 1$
2, 11	Soft Iron (with losses)	0.01	NA	NA
3, 4	NA	0.01	$\mathbf{B} = \mu_0 \mu_r \mathbf{H} + \mathbf{B}_r$	$\mu_r = 1$ $\mathbf{B}_r = (0, 1.3)$
6, 10	NA	0.01	$\mathbf{H} = f( \mathbf{B} )\mathbf{e}_B$	$ \mathbf{H}  =$ $\text{HBFe}(\text{normB\_emqa}[1/T])[\text{A/m}]$

4. Click **Apply** and **OK** to close the **Subdomain Settings** dialog box.

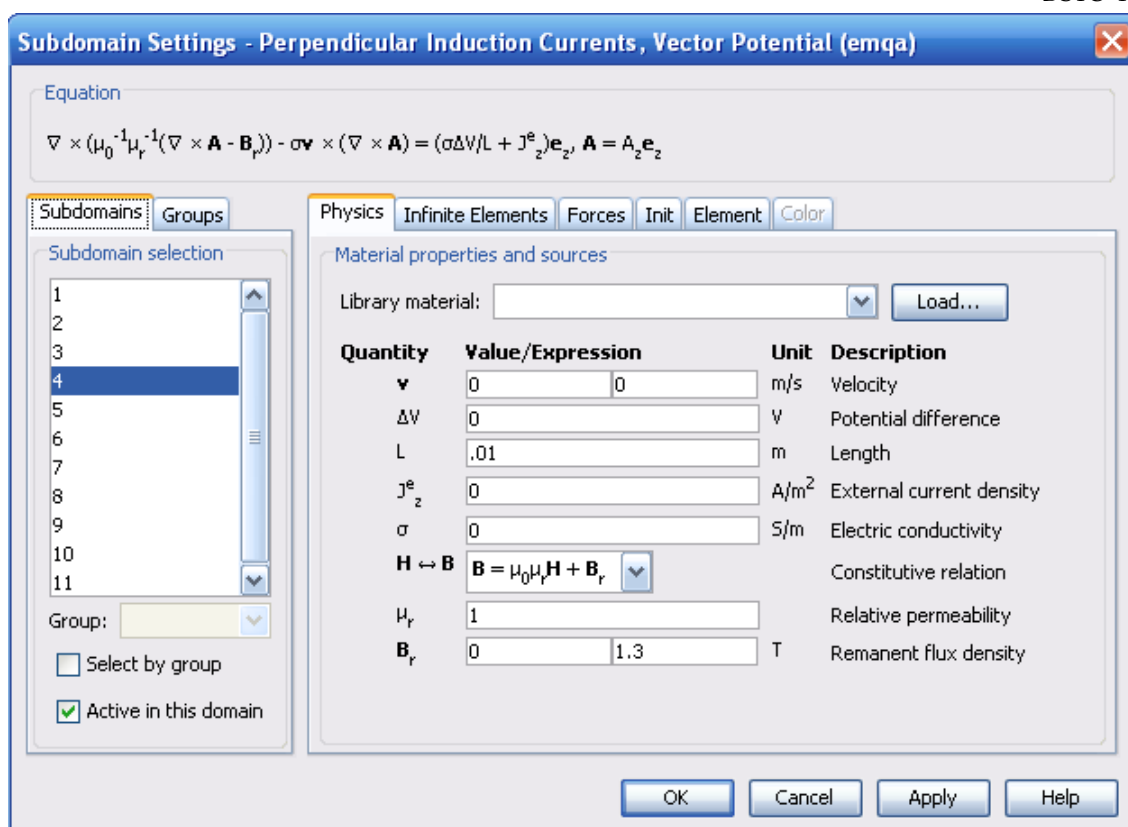


Figure A6. Comsol subdomain settings dialog box

**Subdomain Settings - Plane Strain**

1. From the **Multiphysics** menu, select the **Plane Strain** application mode (see Figure A7).
2. From the **Physics** menu, select **Subdomain Settings**.
3. In the **Subdomain Settings** dialog box, select subdomains 1, 2, 3, 4, 11 and deselect the tick box labeled "Active in this domain".
4. For the other subdomains enter the parameters given in Table A3.

Table A3. Material properties and geometric settings for the harvester model

Subdomains	Library Material	E	V	p	Thickness
5	NA	50E6	0.33	958	0.01
7, 9	NA (see ref. [47])	2.9E6	0.35	3890.2	0.01
8	Lead Zirconate Titanate (PZT-5A)	59E9	0.33	NA	0.01
6, 10	NA	30E9	0.45	7850	0.01

5. For subdomains 6 and 10, click the **Initial Stress and Strain** button and select the tick box labeled "Include initial strain".
6. For **Initial normal strain** type ( $\lambda_x$ ,  $\lambda_y$ , 0).
7. Click **Apply** and **OK** to close the **Subdomain Settings** dialog box.

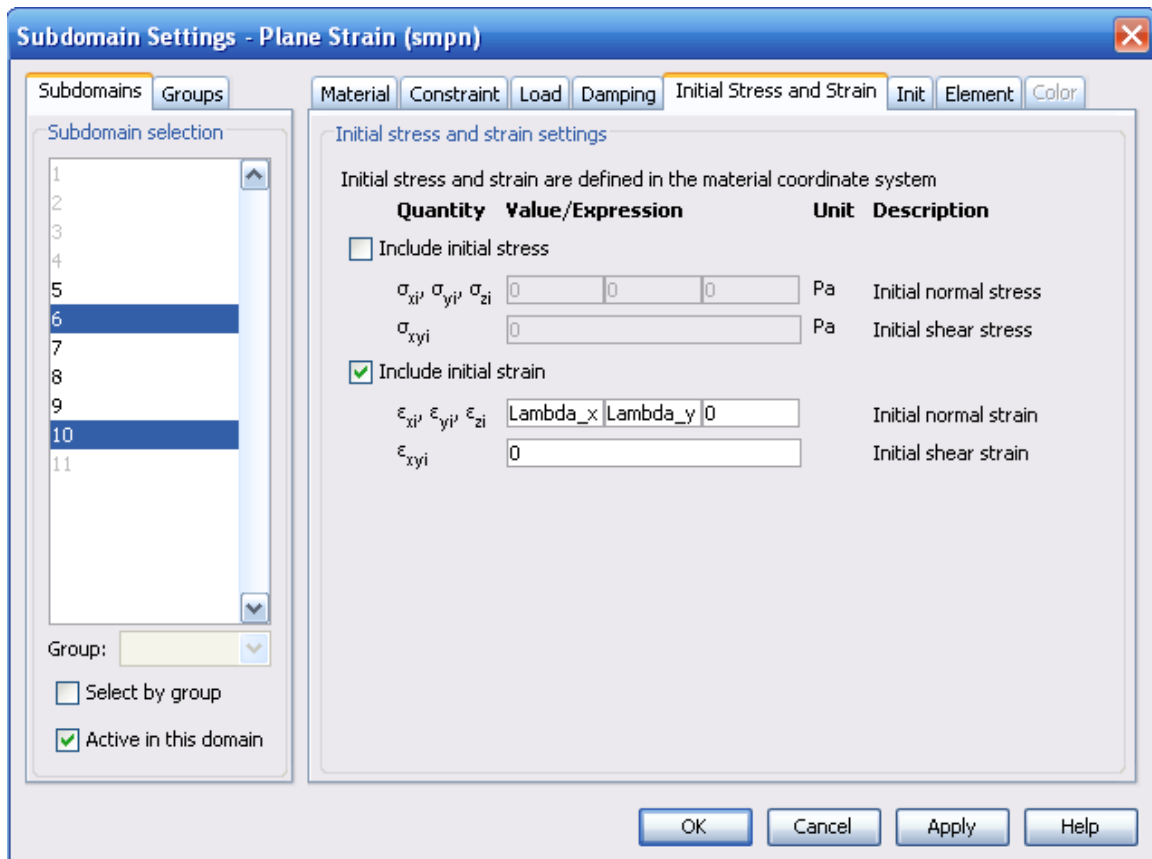


Figure A7. Comsol subdomain settings dialog box, initial stress and strain menu tab

### Boundary Settings – Plane Strain

1. From the **Physics** menu, select **Boundary Settings** (see Figure A8).
2. In the **Boundary Settings** dialog box, select boundaries 12 and 24 and select **Prescribed Displacement** in the **Constraint Condition** list.
3. Under **Standard notation**, select the **R<sub>y</sub>** tick box, and verify the field displays 0.
4. Click **Apply** and **OK** to close the **Boundary Settings** dialog box.

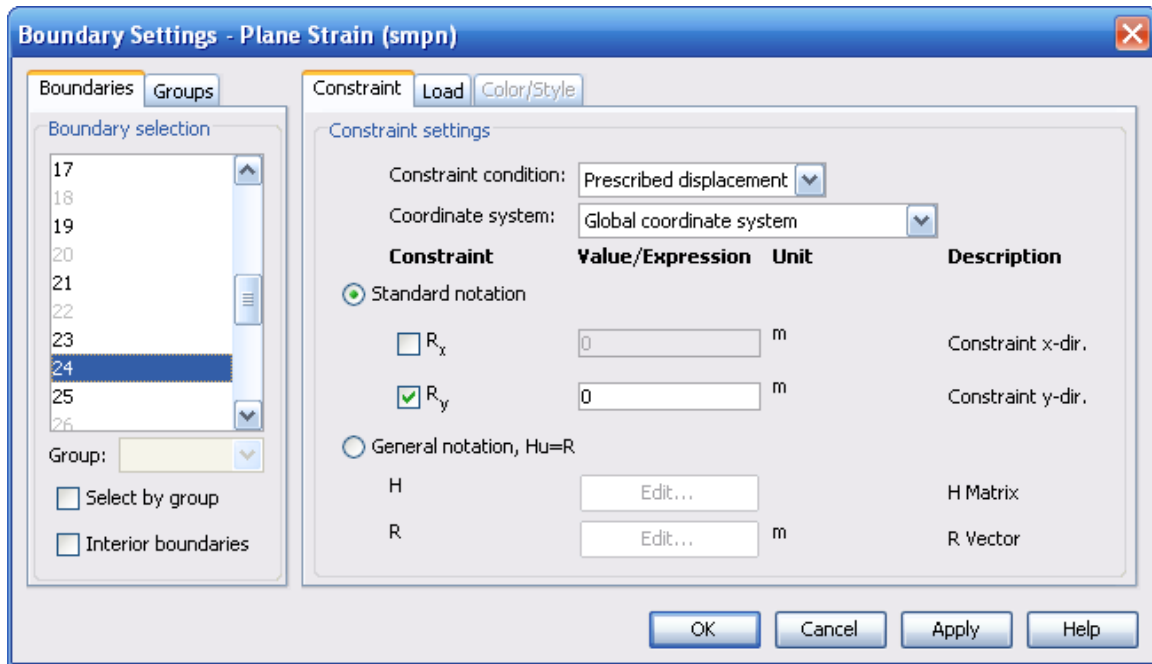


Figure A8. Comsol boundary settings dialog box

#### Point Settings - Plane Strain

1. From the **Physics** menu, select the **Point Settings** (see Figure A9).
2. In the **Point Settings** dialog box, select point 15.
3. Under **Standard Notation**, select the **R<sub>x</sub>** and **R<sub>y</sub>** tick boxes, and verify that the fields display 0.
4. Click **Apply** and **OK** to close the **Point Settings** dialog box.

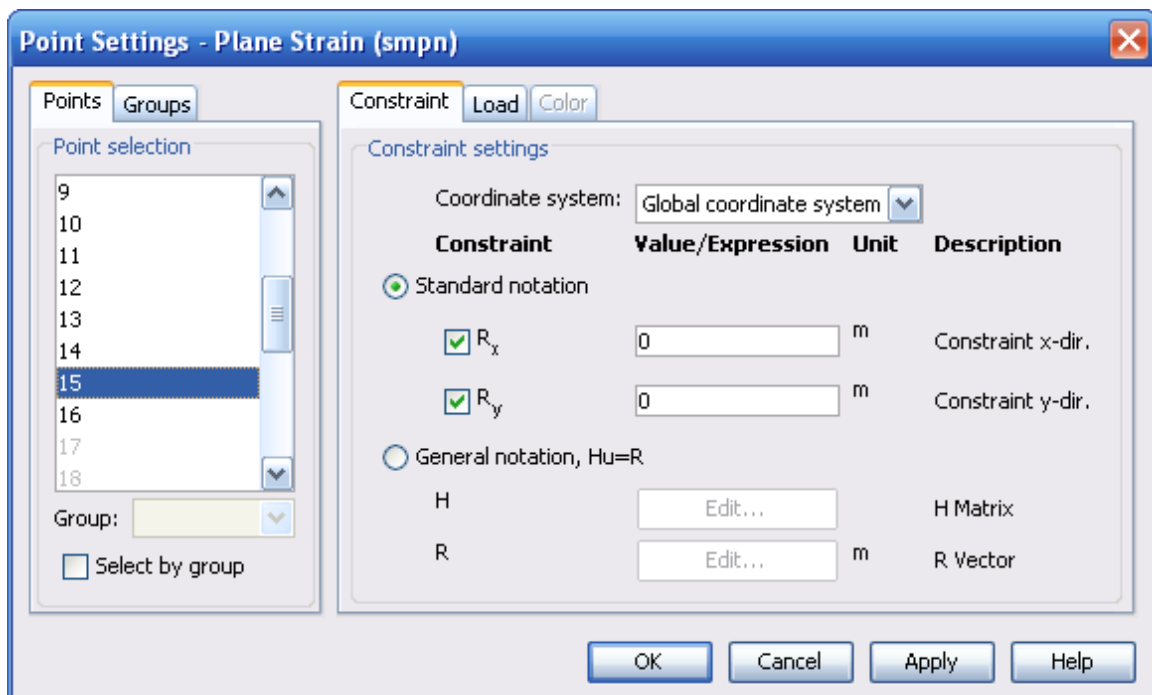


Figure A9. Comsol point settings dialog box

## MATERIALS PROPERTIES

1. From the **Option** menu, open the **Materials/Coefficients Library** dialog box.
2. From the **Materials** area, expand the **Model** heading and select **Soft Iron (with losses)**.
3. From the **All** tab, scroll down the list of coefficients and find **sigma**.
4. Clear the **sigma** edit field and type 0.
5. Click **Apply** and **OK** to close the **Materials/Coefficients Library** dialog box.

## MESH GENERATION

### *Subdomain Properties*

1. From the **Mesh** menu, select **Free Mesh Parameters**.
2. In the **Free Mesh Parameters** dialog box, select the **Subdomain** tab.
3. Select each subdomain and enter the parameters given in Table A4.

Table A4. Mesh settings for harvester model.

Subdomains	Maximum element size	Method
1, 11	NA	Triangle
2, 3, 4	1E-3	Triangle (advancing front)
5, 6, 7, 8, 9, 10	1E-4	Triangle (advancing front)

### *Boundary Properties*

1. In the **Free Mesh Parameters** dialog box, select the **Boundary** tab.
2. Select boundaries 37 and 39, and enter **3E-4** in the **Maximum element size** edit field.
3. Select boundaries 23 and 25, and enter **1E-4** in the **Maximum element size** edit field.
4. Click the **Remesh** button to generate the mesh (as indicated in Figure A10).
5. Click **Apply** and **OK** to close the **Free Mesh Parameters** dialog box.

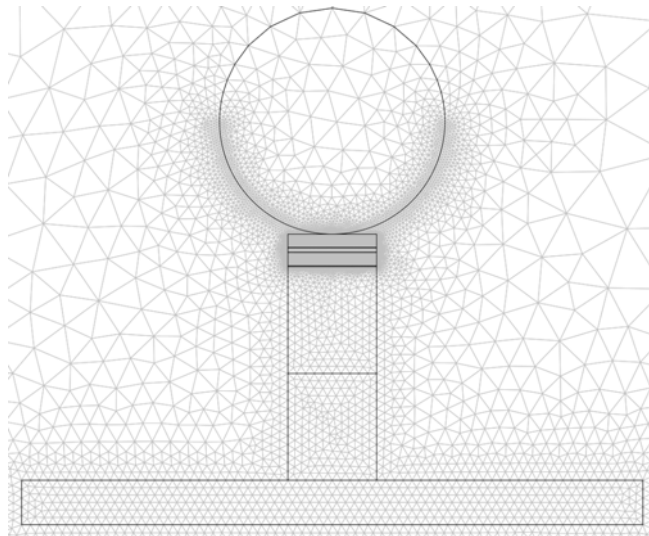


Figure A10. Comsol meshing of the two-dimensional model

## COMPUTING THE SOLUTION

1. From the **Solve** menu, select **Solver Parameters** (see Figure A11).
2. In the **Analysis types** area, select **Static** in the **Perpendicular Induction Current, Vector Potential** list.
3. Verify that in the **Analysis types** area the **Plane Strain** list is also **Static**.
4. Verify that in the **Linear system solver** area and list, **Direct (UMFPACK)** is selected.
5. Click **Apply** and **OK** to close the **Solver Parameters** dialog box.
6. Click the **Solve** button (equal sign) on the Main toolbar to solve the model (or choose **Solve Problem** from the **Solve** menu). Example output is shown in Figure A12.

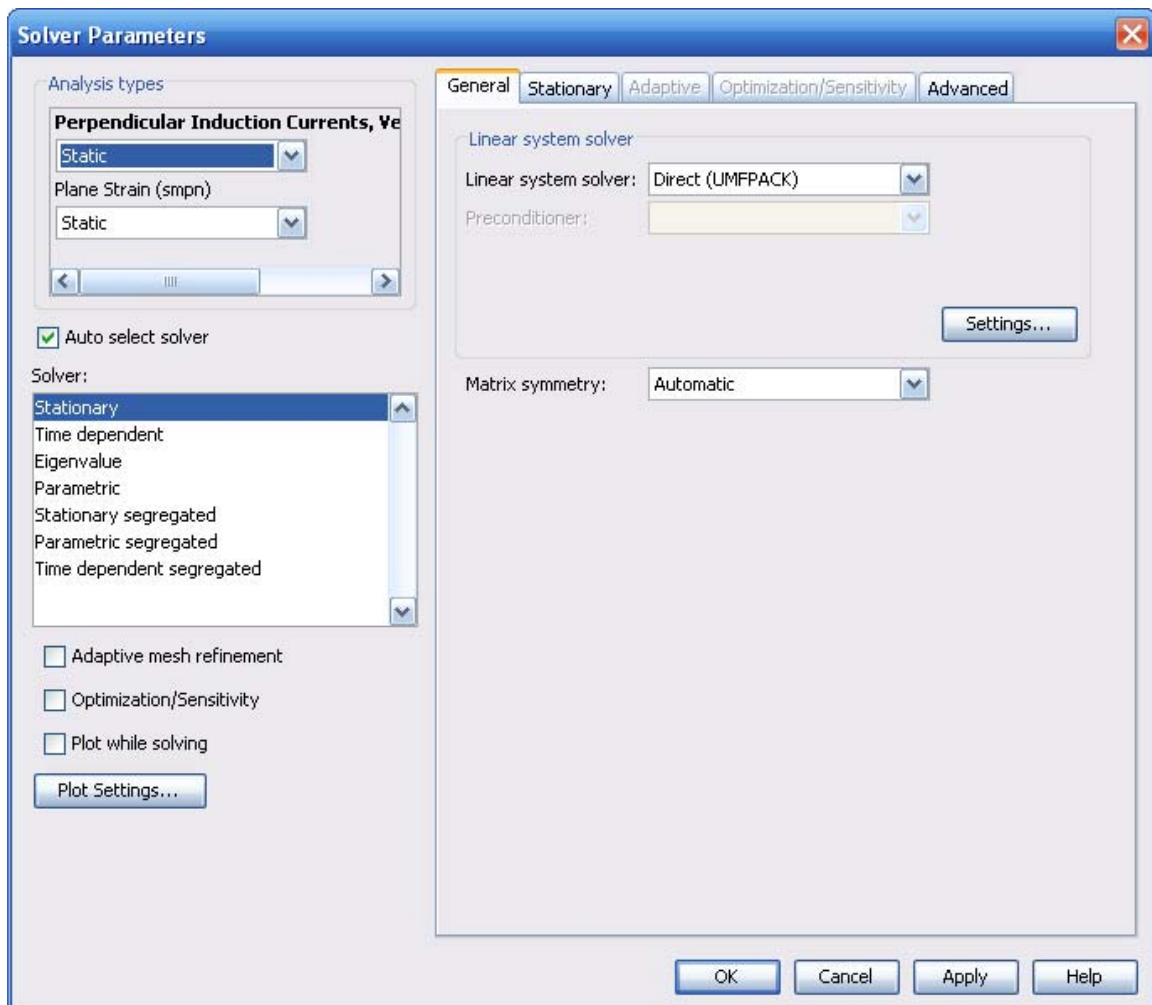


Figure A11. Comsol solver parameters dialog box

## POSTPROCESSING AND VISUALISATION EXAMPLE

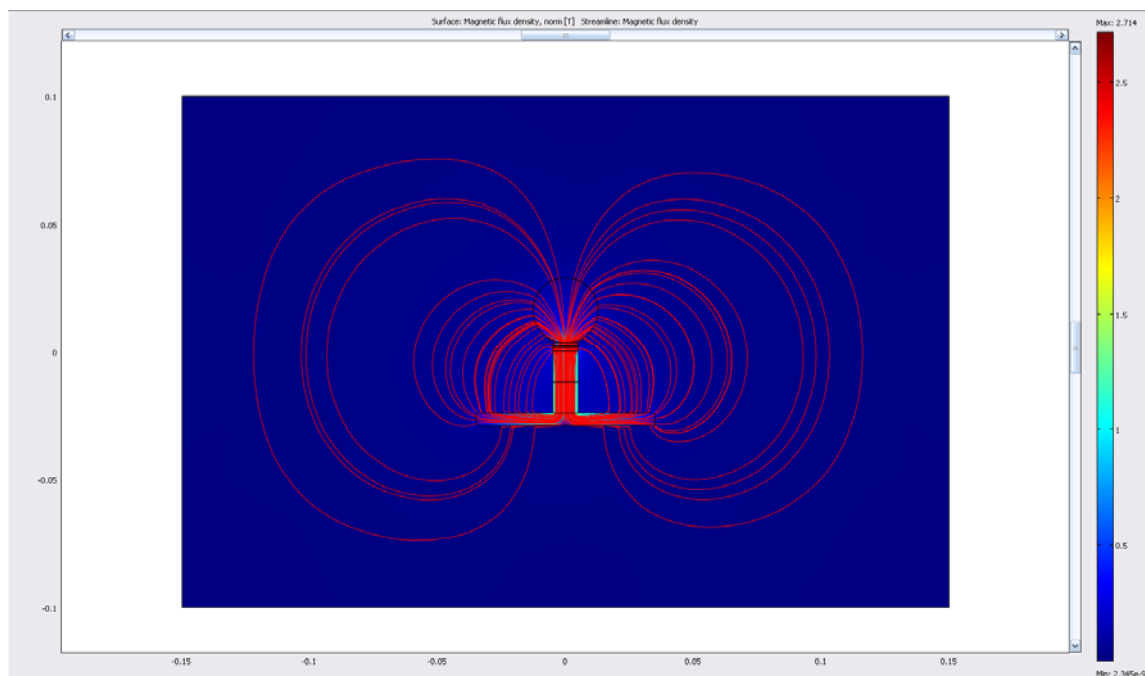


Figure A12. Screen capture using Comsol processing and visualisation



## Appendix B: Three-dimensional modelling

This appendix provides specific details on utilising Comsol multi-physics software [42] to carry out three-dimensional modelling of the bi-axial magnetoelectric vibration energy harvester described in this report. Three-dimensional modelling of the harvester's magnetostrictive (Terfenol-D) elements is done by adapting the two-dimensional approach outlined in reference [44].

Comsol was used to model the three-dimensional forces on the ball-bearing, with the “Magnetostatics, No Currents” application mode from the “AC/DC Module”. Figure B1 shows an example of the geometry and mesh. Both the large cylinder and the large sphere are modelling air as a magnetic conducting environment, and the cylinder has a finer mesh for greater accuracy.

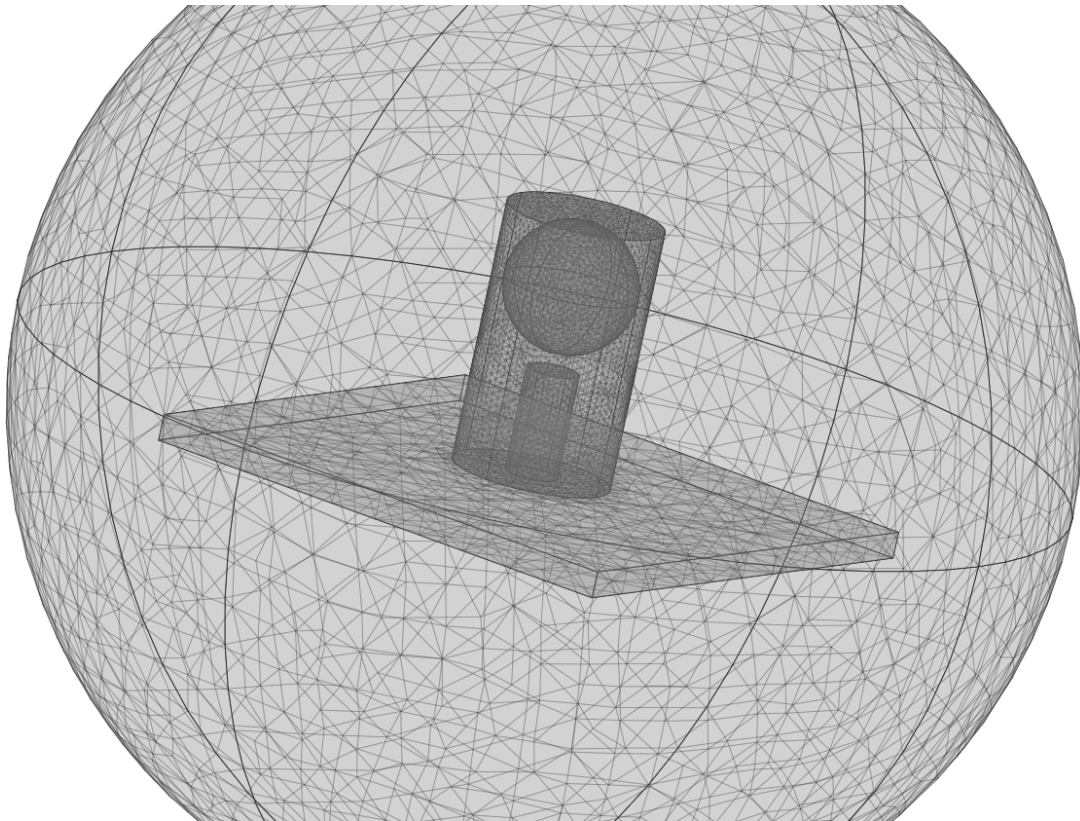


Figure B1. Three-dimensional geometry and mesh used for modelling.

The Matlab interface was used to automate a sweep of different ball bearing positions. The vertical air gap represents the height of the transducer and the ball bearing was swept along the  $y$ -axis to develop the restoring force curve at multiple heights.

The script for these automatic sweeps is included, which repeatedly alters the geometry accordingly, generates a new mesh for this geometry, then solves the model and records the forces. The ball bearing and air cylinder surrounding it are both moved in each cycle, while all other elements remain fixed. The mesh consisted of around 33000 elements and was solved for

around 146000 degrees of freedom; on a machine with 16 GB RAM and a 2.67 GHz CPU a sweep of 91 instances took about 350 minutes to run.

### THREE-DIMENSIONAL MODELLING SCRIPT

```
% JEM_2DpositionSweep
%
% Uses 3D magnetic forces model to solve for a sweep of ball bearing
% positions in a 2D plane.
%
% @version 3.1 - 17/05/2011
% @author Josh McLeod

zShiftSet = .5:.5:3.5;
yShiftSet = 0:.5:4.5;
totalSolNo = length(zShiftSet) * length(yShiftSet);

clc;
j = 0;
solNo = 0;

data2 = {'zShift', 'yShift', 'Fy', 'Fz'};

fprintf('\t\t\t-- 2D POSITION SWEEP --\n\t\t\t\tJosh McLeod\n\n');

% COMSOL version
clear vrsn
vrsn.name = 'COMSOL 3.5';
vrsn.ext = 'a';
vrsn.major = 0;
vrsn.build = 603;
vrsn.rcs = '$Name: $';
vrsn.date = '$Date: 2008/12/03 17:02:19 $';
fem.version = vrsn;

g1=sphere3('.1','pos',{'0','0','0.0125'},'axis',{'0','0','1'},'rot','0');
g3=block3('.1','.1','.005','base','centre','pos',{'0','0','-.0025'},'axis',{'0','0','1'},'rot','0');
g4=cylinder3('.005','.02','pos',{'0','0','0'},'axis',{'0','0','1'},'rot','0');

% Z position loop
for zShift = zShiftSet

    j = j + 1;
    i = 0;
    data(j+1,1) = {'zShift = ', num2str(zShift)};

    fprintf('\nSolving for zShift = %f\n', zShift);

    % Y position loop
    for yShift = yShiftSet

        i = i + 1;
        solNo = solNo + 1;
        if (j==1)
            data(1,i+1) = {'yShift = ', num2str(yShift)};

            if (i==1)
                tic; % start timer to check first solve time
            end
        end

        fprintf('\tyShift = %f\n', yShift);

        % Geometry
        clear draw
        g2=cylinder3('.015','.05','pos',{'0',(yShift/1000),'0'},'axis',{'0','0','1'},'rot','0');
        g5=sphere3('.0127','pos',{'0',(yShift/1000),(.020+.0127+zShift/1000)}, ...
            'axis',{'0','0','1'},'rot','0');

        % Analyzed geometry
        clear s
        s.objs={g1,g2,g3,g4,g5};
        fem.draw=struct('s',s);
```

```

fem.geom=geomcsg(fem);

% Initialize mesh
fem.mesh=meshinit(fem, ...
    'hauto',9, ...
    'hmaxfac',[14,1.5e-3,16,1.5e-3,21,1.5e-3,25,1.5e-3,30,1.5e-3], ...
    'hmaxsub',[1,1e-2,2,1e-2,3,1.5e-3,4,1.5e-3,5,1.5e-3]);

% Application mode 1
clear appl
appl.mode.class = 'MagnetostaticsNoCurrents';
appl.module = 'ACDC';
appl.assignsuffix = '_emnc';
clear bnd
bnd.type = {'Vm0','cont'};
if (yShift==0)
    bnd.ind = [1,1,1,1,2,2,2,2,2,2,2,2,2,2,2,2,2,2,2,2,2,1,1,2,2,2,2,1,2,2, ...
        1,2,2,2];
else
    bnd.ind = [1,1,1,1,1,2,2,2,2,2,2,2,2,2,2,2,2,2,2,2,2,2,1,1,2,2,2,2,1,1,2, ...
        2,2,2,2];
end
appl.bnd = bnd;
clear equ
equ.magconstrel = {'mur','mur','mur','Br'};
equ.M = {{0;0;0},{0;0;0},{0;0;0},{0;0;10e6}};
equ.mur = {1,100,100,1};
equ.maxwell = {{},{},'BB','MM'};
equ.Br = {{0;0;0},{0;0;0},{0;0;0},{0;0;1.3}};
equ.ind = [1,2,1,3,4];
appl.equ = equ;
fem.appl{1} = appl;
fem.frame = {'ref'};
fem.border = 1;
clear units;
units.basesystem = 'SI';
fem.units = units;

% ODE Settings
clear ode
clear units;
units.basesystem = 'SI';
ode.units = units;
fem.ode=ode;

% Multiphysics
fem=multiphysics(fem);

% Extend mesh
fem.xmesh=mesnextend(fem, ...
    'dofversion',1);

% Solve problem
fem.sol=femstatic(fem, ...
    'solcomp',{'Vm'}, ...
    'outcomp',{'Vm'}, ...
    'blocksize','auto', ...
    'linsolver','cg', ...
    'prefun','amg');

% Solution data
force(1)=postint(fem,'BB_forcey_emnc', ...
    'unit','N', ...
    'recover','off', ...
    'dl',23, ...
    'edim',0);

force(2)=postint(fem,'BB_forcez_emnc', ...
    'unit','N', ...
    'recover','off', ...
    'dl',23, ...
    'edim',0);

% Two methods of storing data
data(j+1,i+1) = {force};
data2(solNo+1,:) = {zShift, yShift, force(1), force(2)};

fprintf('\t\t(Fy = %f and Fz = %f)\n', force(1), force(2));

```

```

% Calculate expected completion time
if (j==1 && i ==1)
    currentSolveTime = toc;
    fullSolveTime = currentSolveTime * totalSolNo;

    % Initialise progress bar
    progress = waitbar(solNo/totalSolNo, ...
        ['Test will run for approximately ', int2str(fullSolveTime/60), ...
        ' minutes (has been running: ' int2str(currentSolveTime/60), ' minutes)']);
else
    % Update progress bar
    currentSolveTime = toc;

    waitbar(solNo/totalSolNo,progress, ...
        ['Test will run for approximately ', int2str(totalSolNo/solNo*currentSolveTime/60), ...
        ' minutes (has been running: ' int2str(toc/60), ' minutes)']);
end

end % Y position loop

end % Z position loop

waitbar(1,progress,['Finished in ', int2str(toc/60) ' minutes']);

```

<b>DEFENCE SCIENCE AND TECHNOLOGY ORGANISATION</b> <b>DOCUMENT CONTROL DATA</b>					
				1. PRIVACY MARKING/CAVEAT (OF DOCUMENT)	
2. TITLE  Bi-axial Vibration Energy Harvesting			3. SECURITY CLASSIFICATION (FOR UNCLASSIFIED REPORTS THAT ARE LIMITED RELEASE USE (L) NEXT TO DOCUMENT CLASSIFICATION)  <div style="display: flex; justify-content: space-between;"> <span>Document</span> <span>(U)</span> </div> <div style="display: flex; justify-content: space-between;"> <span>Title</span> <span>(U)</span> </div> <div style="display: flex; justify-content: space-between;"> <span>Abstract</span> <span>(U)</span> </div>		
4. AUTHOR(S)  Scott Moss, Joshua McLeod, Ian Powlesland, Steve Galea			5. CORPORATE AUTHOR  DSTO Defence Science and Technology Organisation 506 Lorimer St Fishermans Bend Victoria 3207 Australia		
6a. DSTO NUMBER DSTO-TR-2649		6b. AR NUMBER AR-015-202		6c. TYPE OF REPORT Technical Report	
7. DOCUMENT DATE July 2012					
8. FILE NUMBER 2011/1064027/1		9. TASK NUMBER CERP 07/388		10. TASK SPONSOR CDS	
				11. NO. OF PAGES 46	
				12. NO. OF REFERENCES 51	
13. DSTO Repository of Publications  <a href="http://dspace.dsto.defence.gov.au/dspace/">http://dspace.dsto.defence.gov.au/dspace/</a>			14. RELEASE AUTHORITY  Chief, Air Vehicles Division		
15. SECONDARY RELEASE STATEMENT OF THIS DOCUMENT  <p style="text-align: center;"><i>Approved for public release.</i></p>					
OVERSEAS ENQUIRIES OUTSIDE STATED LIMITATIONS SHOULD BE REFERRED THROUGH DOCUMENT EXCHANGE, PO BOX 1500, EDINBURGH, SA 5111					
16. DELIBERATE ANNOUNCEMENT  No Limitations.					
17. CITATION IN OTHER DOCUMENTS      Yes					
18. DSTO RESEARCH LIBRARY THESAURUS <a href="http://web-vic.dsto.defence.gov.au/workareas/library/resources/dsto_thesaurus.htm">http://web-vic.dsto.defence.gov.au/workareas/library/resources/dsto_thesaurus.htm</a>  Energy harvesting; Vibration harvesting; Magnetoelectric effect; Magnetostriction/piezoelectric composites; Smart structures; Magnetic devices; Piezoelectric materials; Energy systems.					
19. ABSTRACT This report describes a vibration energy harvesting approach that uses a magnetoelectric (ME) transducer to harvest energy from bi-axial vibrations. The approach is being explored as a potential means of powering in situ structural health monitoring systems embedded within aircraft and other high value engineering assets that experience mechanical vibration. A bi-axial oscillator is created using a permanent-magnet/ball-bearing arrangement, which has the added benefit of permitting a relatively compact design. The magnet produces a bi-axial restoring force on the bearing, and as the bearing oscillates it steers magnetic field through a magnetostrictive/piezoelectric laminate transducer thereby producing an oscillating charge that can be harvested. A simple laboratory demonstrator of a bi-axial ME harvester was created using a Terfenol-D/lead zirconate titanate/Terfenol-D transducer, and was shown to produce a peak rms power of 121 $\mu$ W from an rms acceleration of 61 mG at 9.8 Hz.					